Future Changes of PNA-like MJO Teleconnections in CMIP6 Models: Underlying Mechanisms and Uncertainty

JIABAO WANG,[a] HYEMI KIM,[b] AND MICHAEL J. DEFLORIO[a]

[a] *Center for Western Weather and Water Extremes, Scripps Institution of Oceanography, University of California, San Diego, La Jolla, California*
[b] *School of Marine and Atmospheric Sciences, Stony Brook University, Stony Brook, New York*

(Manuscript received 10 June 2021, in final form 3 February 2022)

ABSTRACT: Future changes in boreal winter MJO teleconnections over the Pacific–North America (PNA) region are examined in 15 Coupled Model Intercomparison Project phase 6 models (CMIP6s) under SSP585 (i.e., Shared Socioeconomic Pathway 5 following approximately the representative concentration pathway RCP8.5) scenarios. The most robust and significant change is an eastward extension (~4° eastward for the multimodel mean) of MJO teleconnections in the North Pacific. Other projected changes in MJO teleconnections include a northward extension, more consistent patterns between different MJO events, stronger amplitude, and shorter persistence; however, these changes are more uncertain and less significant with a large intra- and intermodel spread. Mechanisms of the eastward teleconnection extension are investigated by comparing impacts of the future MJO and basic state changes on the anomalous Rossby wave source (RWS) and teleconnection pathways with a linear baroclinic model (LBM). The eastward extended jet in the future plays a more important role than the eastward-extended MJO in influencing the east–west position of MJO teleconnections. It leads to more eastward teleconnection propagation along the jet due to the eastward extension of turning latitudes before they propagate into North America. MJO teleconnections thus are positioned 2.9° more eastward in the North Pacific in the LBM. The eastward extended MJO, on the other hand, helps to generate a more eastward-extended RWS. However, negligible change is found in the east–west position of MJO teleconnections (only 0.3° more eastward in the LBM) excited from this RWS without the jet impacts. The above results suggest the dominant role of the jet change in influencing future MJO teleconnection position by altering their propagation pathways.

KEYWORDS: Madden-Julian oscillation; Pacific-North American pattern/oscillation; Climate change; General circulation models

1. Introduction

The Madden–Julian oscillation (MJO; Madden and Julian 1971, 1972) is a tropical planetary-scale convectively coupled system with a period of approximately 30–60 days. It travels from the Indian Ocean to the date line where the convective signal often tends to cease, while the circulation component circumnavigates the tropical belt. As the MJO propagates, it influences the extratropics through the generation of an anomalous Rossby wave source (RWS) as a result of interaction between the upper-level MJO divergence and the strong absolute vorticity gradient in the region of the midlatitude North Pacific westerly jet (Sardeshmukh and Hoskins 1988). The excited Rossby waves propagate into the extratropics following great circle paths, modulating circulations therein. For example, about one to two weeks after MJO phase 3 (when the enhanced convection is over the eastern Indian Ocean and suppressed convection is over the western Pacific), a negative Pacific–North America (PNA)-like pattern and a positive North Atlantic Oscillation (NAO) are triggered in the North Pacific and North Atlantic, respectively (e.g., Cassou 2008; Mori and Watanabe 2008; Lin et al. 2009; Tseng et al. 2019; Wang et al. 2020a,b). Changes in these teleconnection patterns further modulate midlatitude weather systems such as blocking events (Henderson et al. 2016), precipitation and temperature (Zhou et al. 2012; Zheng et al. 2018), atmospheric rivers (Mundhenk et al. 2016; Zhou et al. 2021), and storm tracks (Deng and Jiang 2011; Zheng et al. 2018). Impacts of the MJO on the extratropics are reviewed in Stan et al. (2017) and Jiang et al. (2020).

Given the substantial global impacts of MJO teleconnections, efforts have been made to advance our understanding of their intrinsic characteristics in the current climate. Wang et al. (2020a) developed a set of diagnostics for a quantitative examination of MJO teleconnection characteristics and found that when the MJO is in phases 2–3 or 6–7, MJO teleconnections have ~20% stronger amplitude, ~1 week longer persistence, and ~10% more consistent patterns between individual MJO events than the rest of the MJO phases (Wang 2020). Compared to MJO teleconnections in the current climate, only a few studies focused on the projected future changes. Wolding et al. (2017) and Jenney et al. (2021) suggested an overall weaker amplitude of MJO teleconnections over the PNA region due to the increased static stability in future climate based on the linear baroclinic model (LBM). However, a recent study by Zhou et al. (2020), based on eight CMIP5 and three CMIP6 models that produce reasonable MJO characteristics, argued that future changes in MJO teleconnection amplitude over North America are negligible. On the

Denotes content that is immediately available upon publication as open access.

Corresponding author: Jiabao Wang, jiw093@ucsd.edu

DOI: 10.1175/JCLI-D-21-0445.1

other hand, Samarasinghe et al. (2021) found stronger teleconnection amplitude over the Gulf of Alaska and North Atlantic in the Community Earth System Model version 2–Whole Atmosphere Community Climate Model (CESM2-WACCM). Although changes in teleconnection amplitude are uncertain and no consensus exists in recent studies, Zhou et al. (2020) found that MJO teleconnections may extend eastward in the future climate due to an eastward extension of the jet exit, assisted by the eastward MJO extension. This study expands on previous research on MJO teleconnections under the changing climate by further assessing the underlying physical mechanisms and uncertainty in 15 CMIP6 models, which provides a more reliable database given that both MJO propagation (Ahn et al. 2020) and MJO teleconnections (will be shown in this study) are largely improved in CMIP6 compared to CMIP5. Our analysis includes a detailed diagnosis of each MJO phase and examination of the relative impacts of the MJO and basic state on dynamical processes associated with MJO teleconnection generation and propagation. Discussion of the intra- and intermodel uncertainty builds upon the recent work of Jenney et al. (2021), which examined the uncertainty of future MJO teleconnections based on LBM experiments instead of using the direct CMIP6 simulations.

Because MJO teleconnections are modulated by both the MJO and the basic state (e.g., Henderson et al. 2017; Zheng and Chang 2019; Wang et al. 2020b), uncertainty in the future MJO and basic state projections can lead to uncertainty in MJO teleconnection projections. The MJO precipitation is likely to intensify (Bui and Maloney 2018, 2019a,b; Maloney et al. 2019) and propagate farther eastward into the central and eastern Pacific under anthropogenic warming (Subramanian et al. 2014; Chang et al. 2015; Adames et al. 2017). The eastward extension of the MJO propagation depends on the enhanced warming in sea surface temperature (SST) over the climatological warm pool (Zhou et al. 2020). The degree of the MJO eastward extension in individual CMIP models is correlated with the projected west–east warming gradient over the warm pool (Zhou et al. 2020). Changes to the MJO circulation are more uncertain. Some studies showed stronger future MJO circulations (Carlson and Caballero 2016; Pritchard and Yang 2016), while others showed either ambiguous (Liu 2013; Subramanian et al. 2014) or weaker future MJO circulation (e.g., Adames et al. 2017; Bui and Maloney 2018, 2019a,b). Besides changes to MJO characteristics, the North Pacific subtropical jet is likely to become stronger and extend farther eastward in the future (e.g., Neelin et al. 2013; Simpson et al. 2016; Zhou et al. 2020). In this study, future MJO and basic-state changes are revisited in CMIP6s. Possible causes of MJO teleconnection changes from the MJO and basic-state impacts have been discussed in Zhou et al. (2020). Here, we extend their work by further investigating the relative contributions of the MJO and basic state to changes in the anomalous RWS, stationary wavenumber, and teleconnection wave paths with the LBM experiments.

The paper is organized as follows. The GCMs and reference data are introduced in section 2, along with the evaluation of MJO teleconnection simulation skills in CMIP6 models. Future changes in MJO teleconnections are examined in section 3. Future changes in the MJO and basic state are discussed in section 4. Mechanisms of future MJO teleconnection changes are discussed in section 5, followed by a summary and discussion in section 6.

2. Data and methods

We use the daily output from 22 CMIP6 model simulations (Eyring et al. 2016; Table 1) including outgoing longwave radiation (OLR), horizontal winds, precipitation, and geopotential height. All available ensemble members archived in both the historical and ScenarioMIP runs (O'Neill et al. 2016) are used with a total of 76 ensemble members. We use the Shared Socioeconomic Pathway 5 (SSP5)-based RCP scenario from the ScenarioMIP runs, which follows approximately the RCP8.5 global forcing pathway (i.e., high radiative forcing of 8.5 W m^{-2} by the end of the twenty-first century) with SSP5 socioeconomic conditions (i.e., fossil-fueled development; herein called SSP585). We use this extreme scenario to obtain more significant signals of future changes. The historical and projected future simulations cover the periods of 1979–2014 and 2065–2100, respectively. This equivalent 36-yr period allows for a consistent comparison between the current and future climate. All the datasets are interpolated to a common grid of 2.5° × 2.5° to facilitate consistent multimodel analysis.

The reference OLR data are derived from the NOAA Advanced Very High-Resolution Radiometer (AVHRR; Liebmann and Smith 1996) product dataset, while other variables are mainly from the ECMWF ERA5 reanalysis dataset (Hersbach et al. 2020). The reference data period is from 1979 to 2018. To examine the inter-reanalysis spread of the observational MJO teleconnection pattern, we also analyzed geopotential height from the other three reanalysis datasets that covers similar periods: 1) NCEP Climate Forecast System reanalysis (CFSR; Saha et al. 2010) from 1979 to 2010, 2) version 2 of the NASA Modern-Era Reanalysis for Research and Applications (MERRA-2; Molod et al. 2015) from 1980 to 2018, and 3) the Japanese 55-Year Reanalysis (JRA-55; Kobayashi et al. 2015) from 1979 to 2018. We focus our analysis from October to March when both the MJO and its teleconnections are most prominent. Anomalies are derived by removing the first three harmonics of the annual cycle, then applying a 25–90-day bandpass filter to extract the intraseasonal signal.

The real-time multivariate MJO (RMM; Wheeler and Hendon 2004) indices are used to define the phase and amplitude of the MJO. RMM indices are the first two leading principal components (RMM1 and RMM2) of the combined empirical orthogonal functions (CEOFs) constructed using 15°S–15°N averaged OLR and 850- and 250-hPa zonal wind anomalies. For a consistent comparison, the model RMM indices are obtained by projecting their OLR and zonal wind anomalies onto the observed CEOF eigenvectors following Henderson et al. (2017) and Wang et al. (2020a,b). Normalization by the observed global variance is applied before calculating the RMM indices. This study focuses on MJO

TABLE 1. Description of CMIP6 models (CMIP6s) used in this study. Models in bold are 15 "good" MJO teleconnection models. The "Ensemble members" column lists the total number of ensemble members that are initially analyzed in this study, which apply to Figs. 1 and 2. The number of selected ensemble members for the study of future changes is indicated in parentheses. (Expansions of acronyms are available online at http://www.ametsoc.org/PubsAcronymList.)

	Model	Modeling center	Ensemble members
1	**ACCESS-CM2**	CSIRO-ARCCSS, Australia	1 (1)
2	**CESM2**	NCAR, United States	2 (2)
3	**CESM2-WACCM**		3 (3)
4	**CNRM-CM6-1**	CNRM-CERFACS, France	6 (4)
5	**CNRM-ESM2-1**		3 (2)
6	**EC-Earth3**	EC-Earth-Consortium, Italy	4 (1)
7	**FGOALS-g3**	CAS, China	3 (3)
8	**GFDL-CM4**	NOAA-GFDL, United States	1 (1)
9	**HadGEM3-GC31-LL**	MOHC, United Kingdom	4 (2)
10	**HadGEM3-GC31-MM**		3 (1)
11	**MIROC6**	MIROC, Japan	3 (2)
12	**MPI-ESM1-2-HR**	DKRZ, Germany	2 (1)
13	**MPI-ESM1-2-LR**	MPI-M, Germany	10 (8)
14	**MRI-ESM2-0**	MRI, Japan	1 (1)
15	**UKESM1-0-LL**	MOHC, United Kingdom	5 (4)
16	BCC-CSM2-MR	BCC, China	1
17	CanESM5	CCCma, Canada	14
18	CNRM-CM6–1-HR	CNRM-CERFACS, France	1
19	IPSL-CM6A-LR	IPSL, France	5
20	INM-CM5-0	INM, Russia	1
21	KACE-1-0-G	NIMS-KMA, South Korea	2
22	TaiESM1	AS-RCEC, Taiwan	1

teleconnections in response to strong MJO events defined as having RMM amplitude ($\sqrt{\text{RMM1}^2 + \text{RMM2}^2}$) greater than one.

In this study, MJO teleconnections are defined as the composites of 500-hPa geopotential height anomalies (Z500a) averaged over 5–9 days after each MJO phase, given that it takes about 1–2 weeks for tropically forced Rossby waves to reach the extratropics (Hoskins and Karoly 1981). The Z500a and OLR anomalies (OLR at day 0) in response to MJO phase 3 in the 22 CMIP6 historical runs are compared with ERA5 in Fig. 1. Results for MJO phase 3 are displayed because of its relatively strong impact on the extratropics compared to other phases (Stan et al. 2017; Tseng et al. 2019). A two-tailed Student's *t* test is used to test the significance of the results. The degrees of freedom are defined as the number of days in each MJO phase bin divided by 5 days (the average duration of an MJO phase), following Wang et al. (2020a). Similar to CMIP5 models (Wang et al. 2020a), the positive Z500a over the North Pacific region is well captured by most of the CMIP6 models, while some CMIP6s are unable to capture realistic Z500a over North America (e.g., CNRM-CM6-1, EC-Earth3, HadGEM3-GC31-LL, and MPI-ESM1-2-HR/LR).

MJO teleconnection patterns and amplitudes in various reanalysis datasets and models are compared in the Taylor diagram (Taylor 2001) in Fig. 2. Both the pattern correlation coefficient (pattern CC; curve axis) and relative amplitude (*x* and *y* axes) are calculated using the 5–9-day averaged Z500a composites over the PNA region (120°E–60°W, 20°–80°N) with respect to ERA5. The results are shown for MJO phases 3 and 7 and an average of all MJO phases. The relative amplitude is defined as the Z500a variance in CMIP6, CFSR, MERRA-2, and JRA-55 divided by Z500a variance in ERA5, following Wang et al. (2020a). Values larger (smaller) than 1.0 represent stronger (weaker) MJO teleconnection amplitude than ERA5. Compared to CMIP5 (Fig. 2 in Wang et al. 2020a), simulation of the MJO teleconnection pattern is overall improved in CMIP6. The pattern CC of the multimodel mean (MMM) MJO teleconnections averaged across all MJO phases is 0.59 in 22 CMIP6 models and is 0.53 in 22 CMIP5 models. The teleconnection amplitude is closer to the reanalysis in CMIP6s than CMIP5s, although most models still overestimate the amplitude. The MMM relative amplitude is 1.38 in CMIP6 and is 1.42 in CMIP5 averaged across all MJO phases. The spread in teleconnection patterns between different reanalyses is small for MJO phases 3 and 7 (pattern CC ~0.9) but is larger for other phases, such as phases 1 and 5 (pattern CC ~0.4; not shown).

To understand the future changes of MJO teleconnections, we select models and their ensembles among the 22 CMIP6 models that meet the following criteria: 1) teleconnection pattern CC > 0.5 for the average across all MJO phases and 2) pattern CC > 0.5 for both MJO phases 3 and 7. A pattern CC of 0.5 is the threshold for 95% significance in the PNA region. A total of 15 models and 36 ensembles (bold in Table 1 and starred in Fig. 1, respectively) that meet both criteria are selected.

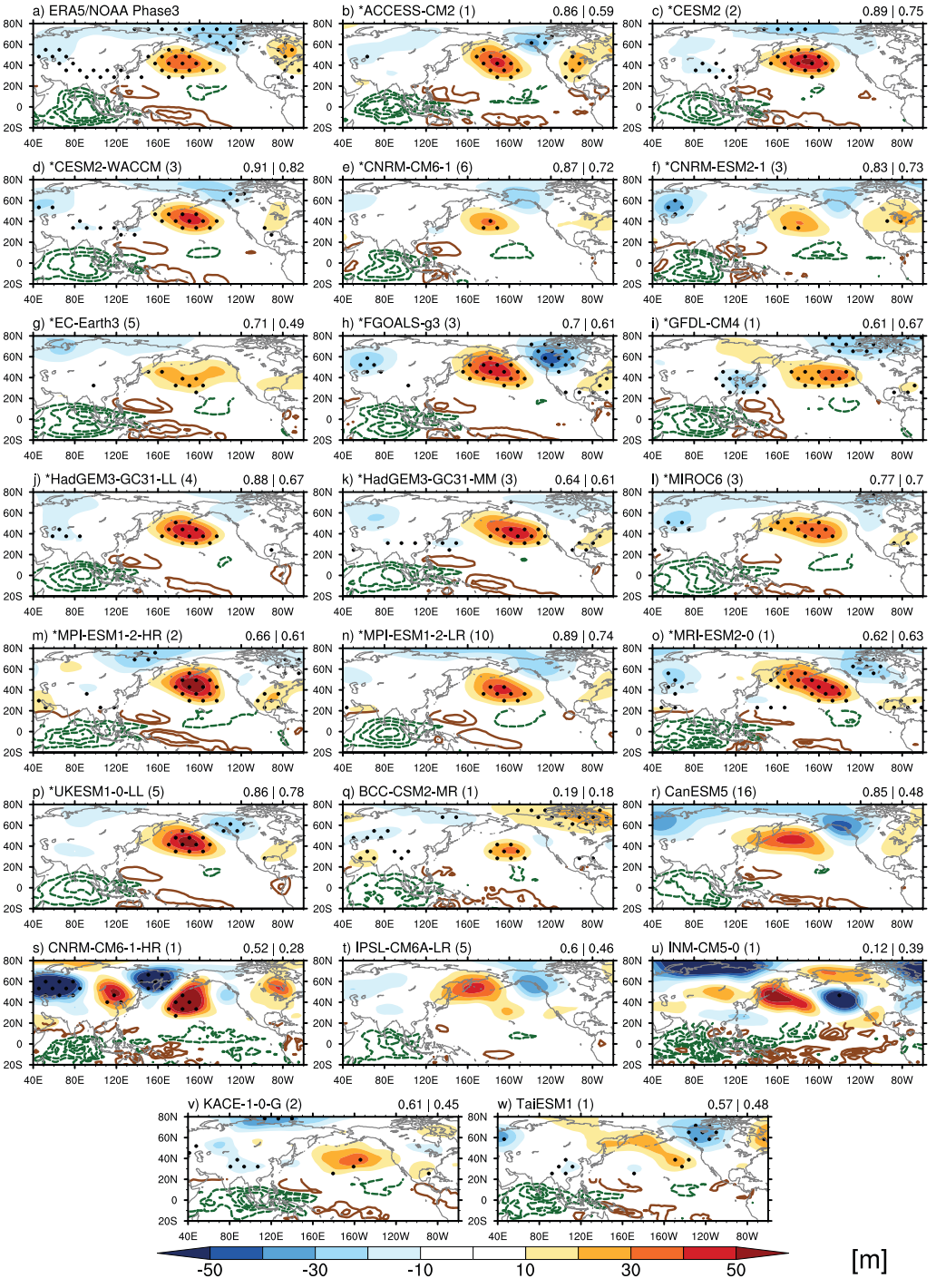

FIG. 1. The 5–9-day averaged lagged response of filtered Z500a (shading; m) to MJO phase 3 [OLR contour: green (brown) represents enhanced (suppressed) convection, interval: 10 W m^{-2}] in (a) ERA5/NOAA and (b)–(w) 22 CMIP6 historical runs. OLR anomalies are shown for day 0. The dotted areas represent significant Z500a exceeding the 95% confidence level according to the two-tailed Student's *t* test. The ensemble mean is presented if there are multiple ensemble members for a particular model. Values on the top right of each figure denote the Z500a pattern CC calculated between ERA5 and models over the PNA region 120°E–60°W, 20°–80°N (left for MJO phase 3, right for an average of all MJO phases). Models with a star are the "good" MJO teleconnection models selected based on the criteria defined in section 2.

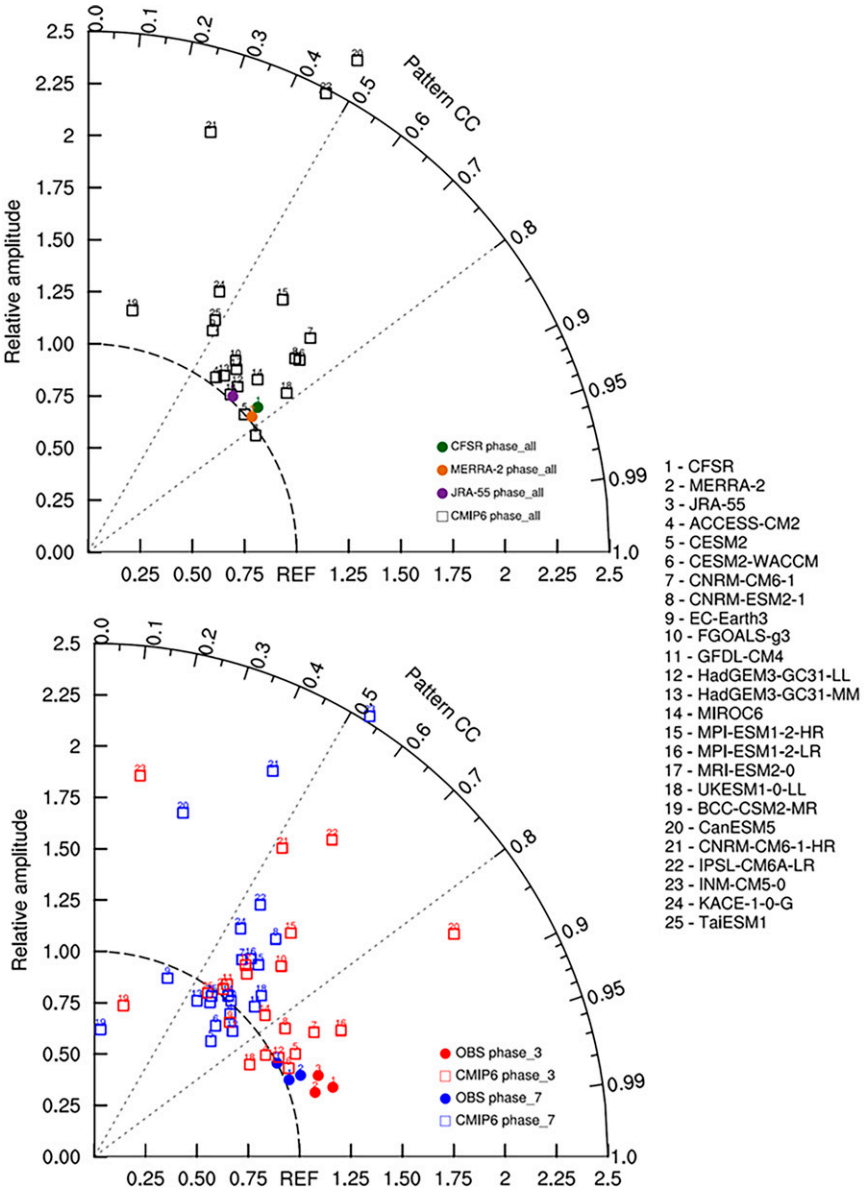

FIG. 2. Taylor diagrams of Z500a over the PNA region for the (top) average across all MJO phases and (bottom) phases 3 and 7. Pattern CC and relative amplitude calculated with respect to ERA5 are shown at the curve axis and the *x* and *y* axes, respectively. Squares indicate the CMIP6s (ensemble mean is presented if there are multiple ensemble members for a particular model), and dots indicate the reanalysis datasets (CFSR, MERRA-2, and JRA-55). The distance between each dot/square and the reference point "REF" indicates the root-mean-square error (RMSE).

3. Uncertainty of future changes in MJO teleconnections

The MJO phase 3 Z500a values in the selected models are compared between the historical and SSP585 (hereafter referred to as "future") runs (Fig. 3). Both the MMM and individual models are shown. To ensure an equal weighting between the models, the average is first taken over the ensemble members for each model before calculating the MMM. The overall spatial structure of the MMM (Figs. 3a,b) is consistent with Zhou et al. (2020): in the future climate, MJO teleconnections shift eastward while the change in amplitude is close to zero when averaged over the PNA region (due to the cancellation between stronger amplitude over the North Pacific and weaker amplitude over North America). However, the uncertainty of projected changes is evident in individual models (Figs. 3c–ff). For example, CNRM-ESM2-1, EC-Earth3, MPI-ESM1-2-HR, and HadGEM3-GC31-MM project a stronger amplitude over North America, which opposes the MMM.

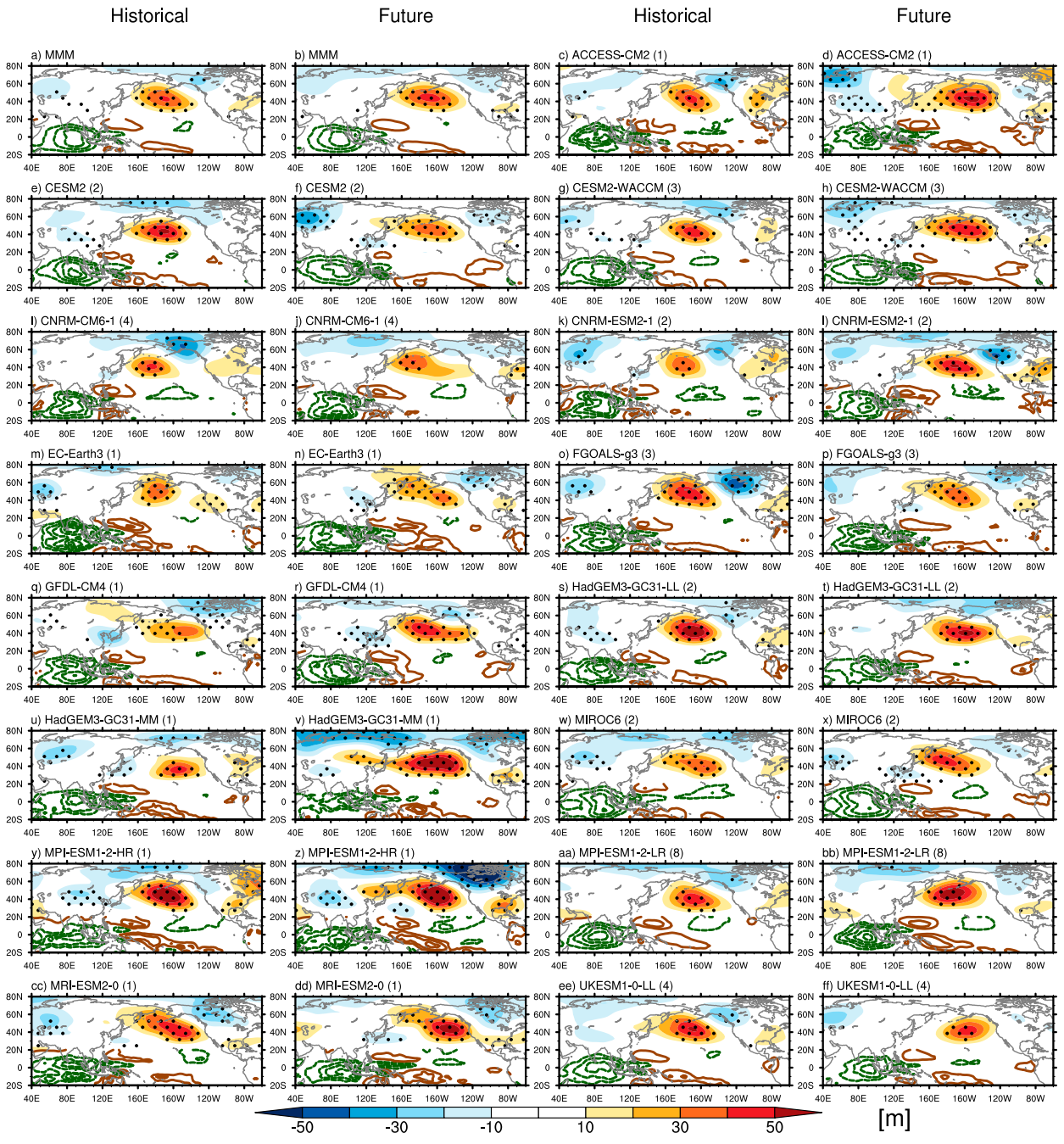

FIG. 3. As in Fig. 1, but for a comparison between the CMIP6 historical and future runs. Values in the parentheses indicate the number of ensemble members selected for the analysis of future MJO teleconnection changes.

The teleconnection changes are quantitatively measured by applying the teleconnection metrics developed in Wang et al. (2020a). Aside from the amplitude and position changes, changes in intraphase pattern consistency (consistency of teleconnection pattern between different MJO events within the same phase, which indicates the uncertainty due to internal variability) and persistence (time duration teleconnections persist before decaying) are also examined [details in Wang et al. (2020a)]. Results for the MMM of each teleconnection metric over the historical period are shown in Table 2 for each MJO phase, along with their comparison with ERA5. The difference of the metric value between future and historical (future minus historical) runs represents the absolute change. A moving-block bootstrapping test with a replacement procedure (Henderson et al. 2016; Wolding et al. 2017) is applied to all models to assess the significance of MJO

TABLE 2. Multimodel mean (MMM) of the teleconnection metrics over the historical period for individual MJO phases from phase 1 (P1) to phase 8 (P8). Results of ERA5 are also listed in parentheses for comparison.

	P1	P2	P3	P4	P5	P6	P7	P8
Amplitude (m)	13.3 (11.3)	18.6 (17.2)	17.2 (14.5)	13.7 (12.2)	14.5 (9.6)	17.8 (13)	17.5 (16.4)	13.5 (10.3)
East–west position (°)	178.6 (174)	184.9 (177)	187.3 (184)	178.1 (173)	184.7 (167)	186.8 (180)	192.6 (175)	188 (170)
Consistency (%)	18.5 (14.2)	28.6 (25.6)	25.5 (17.9)	18.7 (14.6)	19.7 (11.2)	27.8 (14.6)	25.5 (29.6)	18.7 (13.7)
Persistence (day)	9 (8)	12 (15)	12 (11)	10 (9)	10 (8)	12 (10)	12 (13)	10 (9)

teleconnection changes and the uncertainty of the ensemble mean. The bootstrapping procedure is repeated 1000 times to obtain a sufficiently large sample size and the 2.5 and 97.5 percentile values are used to define the 95% confidence interval. If there are multiple ensembles in a model, the bootstrapping data are derived by randomly selecting samples from each different ensemble member without overlap to calculate the ensemble mean. The results are significant if the confidence interval is not encompassing the zero line (e.g., gray bars in Fig. 4).

Changes in the amplitude of MJO teleconnections in individual ensemble members (open circles) and MMM are shown in Fig. 4a for MJO phase 3, along with the 95% confidence interval. The MMM for the average across all MJO phases is also shown. The MMM indicates a slightly stronger teleconnection amplitude over the entire PNA region, which is not significant in most models except in CNRM-ESM2-1, HadGEM3-GC31-MM, and MPI-ESM1-2-HR/LR. This negligible change may be due to the large spread among the models and ensembles (ranges of −10 to 14 m). Even ensembles from the same model project opposite change (such as in CESM2-WACCM, CNRM-CM6-1, HadGEM3-GC31-LL, and MPI-ESM1-2-LR). MJO teleconnection amplitude changes also have strong regional variations, which will be discussed later. The MMM absolute change for all eight MJO phases is shown in Fig. 5a. The percentage (%) values shown on top of each bar indicate the agreement of the projected changes between the models (i.e., multimodel agreement). For example, for phase 1, MMM projects ~2 m (~15% when divided by the historical MMM in Table 2) stronger amplitude in the future, and 67% of models agree with the sign of change. Again, the MMM and percentage of agreement are derived by considering the equal weighting to each model. The meaning of bars in Fig. 5 is different from that in Fig. 4. The bar is striped when the change is significant over 90% confidence level in that MJO phase determined by the bootstrapping test. When averaged across all MJO phases, the teleconnection amplitude over the PNA region will be slightly stronger (~0.36 m; ~2%) in the future and the stronger amplitude is only significant in MJO phase 2.

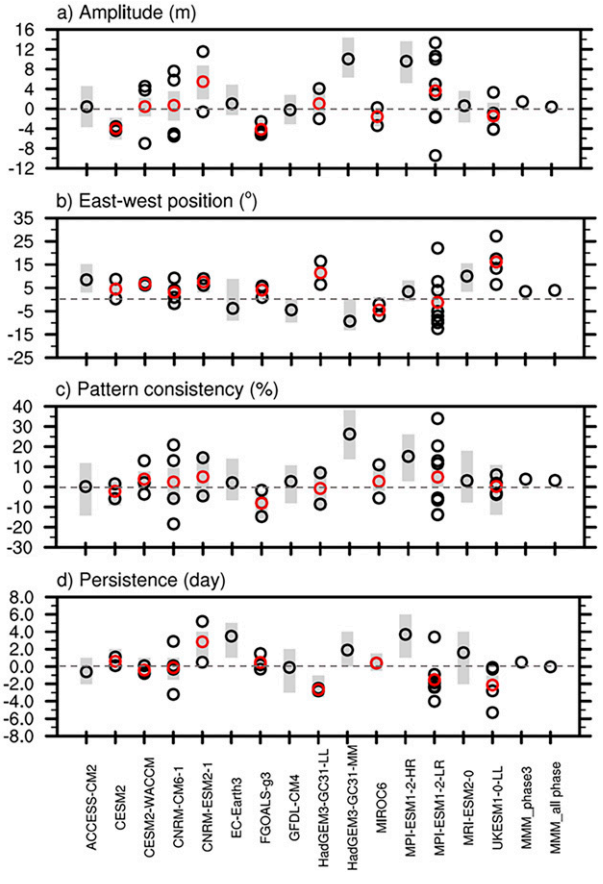

FIG. 4. Absolute change (future minus historical) of phase 3 MJO teleconnection (a) amplitude, (b) east–west position, (c) pattern consistency, and (d) persistence over the PNA region. Black open circles represent the results for individual ensembles or the MMM. Red open circles indicate the ensemble mean. Gray bars indicate the 95% confidence interval of the bootstrapping test.

The spatial distribution of MJO teleconnection change over the PNA region is examined by first creating a future–historical difference map of MJO-related Z500a for each model and then calculating the sign agreement between them (Fig. 6). Regions with red (blue) color shading indicate significantly stronger (weaker) MJO teleconnections in the future. Over the North Pacific, most MJO phases are associated with projected MJO teleconnection changes that have a significant northeastward extension (e.g., phases 2–4 and 6–7), while over the northwestern and northeastern North America most models project weaker MJO teleconnections in the future for phases 3–4 and 6–8. Although consistent changes are found between models in some areas, a large portion is white, indicating a large model spread (uncertainty) of MJO teleconnection changes, especially for phases 1, 4, 5, and 8. Given the large uncertainty between model projections, along with substantial regional differences, conclusions from previous studies that MJO teleconnections will be weaker over the entire PNA region should be interpreted cautiously, as they rely mostly on a single model or idealized model experiments (e.g., Wolding et al. 2017; Jenney et al. 2021).

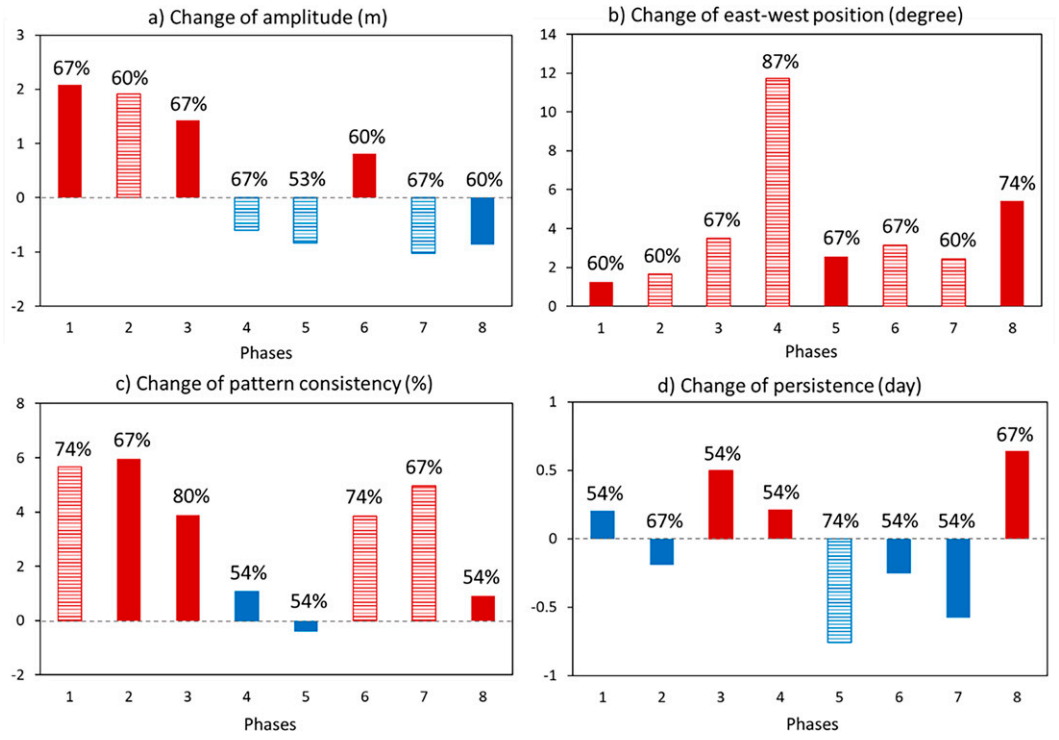

FIG. 5. MMM absolute change of MJO teleconnection (a) amplitude, (b) east–west position, (c) pattern consistency, and (d) persistence for the eight MJO phases. The color of the bar is determined by the percentage of sign agreement rather than the metric value. For example, in (c), the metric value of phase 4 indicates higher pattern consistency (change of MMM is positive), but more models (54%) project a lower pattern consistency, and thus the color of the bar is assigned to blue rather than red. Therefore, red bars represent more models project (a) stronger amplitude, (b) more eastward position, (c) higher pattern consistency, and (d) longer persistence of MJO teleconnections, and vice versa for blue bars. The value on top of each bar indicates the percentage of simulations that agree with the sign of the change. Significant changes greater than 90% confidence level based on the bootstrapping test are indicated as striped bars.

The eastward extension of MJO teleconnections over the North Pacific is further quantified by calculating the difference of teleconnection east–west position between future and historical runs for each ensemble (Fig. 4b). The east–west position is defined as the Z500a weighted longitude, which is computed by the sum of longitude multiplied by Z500a and divided by the sum of Z500a across all longitudes within a 100° × 20° box over the Pacific anomaly cell (Fig. 4 in Wang et al. 2020a). The region for the calculation varies for different MJO phases because of the movement of Pacific Z500a but is generally within the region of 100°E–100°W, 20°–60°N for all phases. A positive (negative) metric value indicates an eastward (westward) extension of MJO teleconnections in future climate. It is found that most models (~67%) project an eastward extension of MJO teleconnections in the future for MJO phase 3 with the largest magnitude difference at 30° in one ensemble of UKESM1-0-LL (Figs. 3ee, 3ff, and 4b). The bootstrapping results are also positively skewed in most models (e.g., ACCESS-CM2, CESM2, CESM2-WACCM). All MJO phases tend to produce ~1°–12° eastward-extended MJO teleconnections in the future with large consistency among the models (Fig. 5b). The eastward extension is especially significant in phases 2–4 and 6–7. To quantify the northward extension in MJO teleconnections indicated in Fig. 6, a similar calculation is employed by changing the Z500a weighted "longitude" to "latitude" over the same region (i.e., the sum of latitude multiplied by Z500a and divided by the sum of Z500a across all latitudes). The MMM indicates an additional northward extension of ~1° for MJO teleconnections averaged across all MJO phases and is significant for MJO phases 2–3 and 6–7 (shifts ~1.3° farther northward; not shown). Note that the metric we used here is an indicator of the effective shift of the Pacific anomaly cell as it is the weighted average of the anomaly and may not represent the exact amount of the degrees that the anomaly shifts (e.g., the outmost boundary of the Pacific anomaly cell). The results thus only suggest that the northward extension is in agreement by most CMIP6 models while less detectable than the eastward extension.

We also examined changes in the MJO teleconnection consistency and persistence. It is found that 80% of model simulations project more consistent (value > 0) MJO teleconnections in the future, such as CESM2-WACCM, CNRM-CM6-1, HadGEM3-GC31-MM, and MPI-ESM1-2-LR (Fig. 4c) for MJO phase 3, and a significantly larger pattern consistency is found for MJO phases 1, 6, and 7 (Fig. 5c). When averaged over all MJO

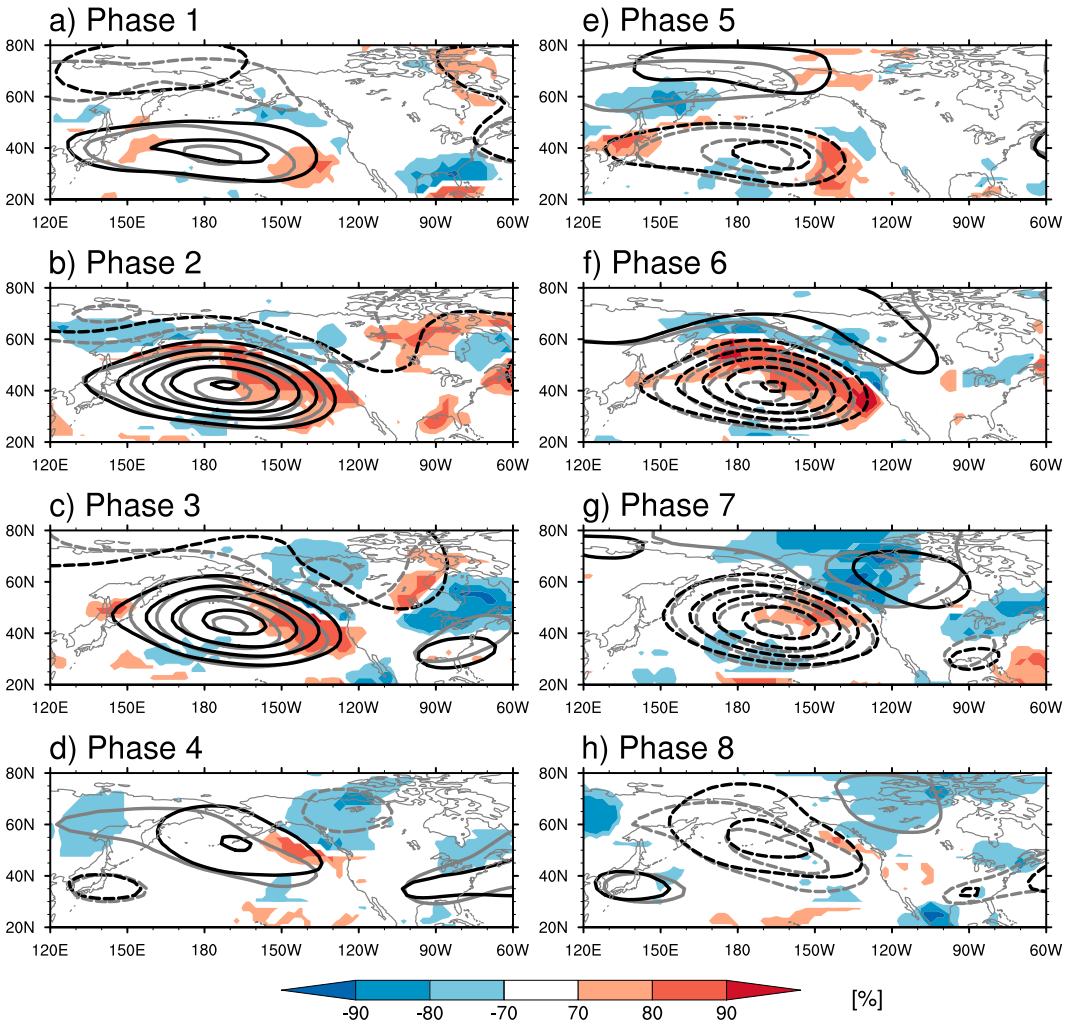

FIG. 6. The 5–9-day averaged lagged response of Z500a to eight MJO phases for the historical MMM (gray contour, interval: 5 m) and future MMM (black contour, interval: 5 m). Shadings indicate the regions where most models (>70%, significant over 90% confidence level) produce a stronger (red) or weaker (blue) amplitude of MJO teleconnections in the future. For example, positive shading in negative Z500a represents a stronger negative Z500a. The percentage of sign agreement is shown by the bottom label bar (a minus sign is added in front of the percentage to represent results for the weaker amplitude).

phases, teleconnections will be ~14% more consistent between different MJO events in the future (absolute change divided by the historical mean), suggesting the potential for a more reliable prediction of future MJO teleconnections. On the other hand, changes in teleconnection persistence are very uncertain between the different MJO phases (Fig. 5d). Phases 3, 4, and 8 are projected to excite longer-persistent MJO teleconnections in the future (value > 0), while the other phases have opposite projections.

In summary, the most significant and robust change in future MJO teleconnections is an eastward extension in the North Pacific, followed by a northward extension and higher pattern consistency. The change in teleconnection amplitude has large uncertainty and the change in persistence is negligible.

4. Future changes in the MJO and basic state

To better understand the impact of the MJO on teleconnections, the overall MJO activity is examined based on the standard deviation of filtered daily precipitation and 850-hPa zonal wind (U850) anomalies over the historical and future period for each model and ensemble. Fewer models (14 models instead of 15) and ensembles (31 ensembles instead of 36) are used due to the limited availability of daily precipitation output. Figure 7 shows the MJO activity for the historical MMM and the difference between the future and historical MMM. The pattern of historical MJO precipitation activity is similar to observations (Fig. 3 in Waliser et al. 2009) with maximum activity over the Indo-Pacific warm pool in boreal winter (Fig. 7a). However, the distribution of MJO wind

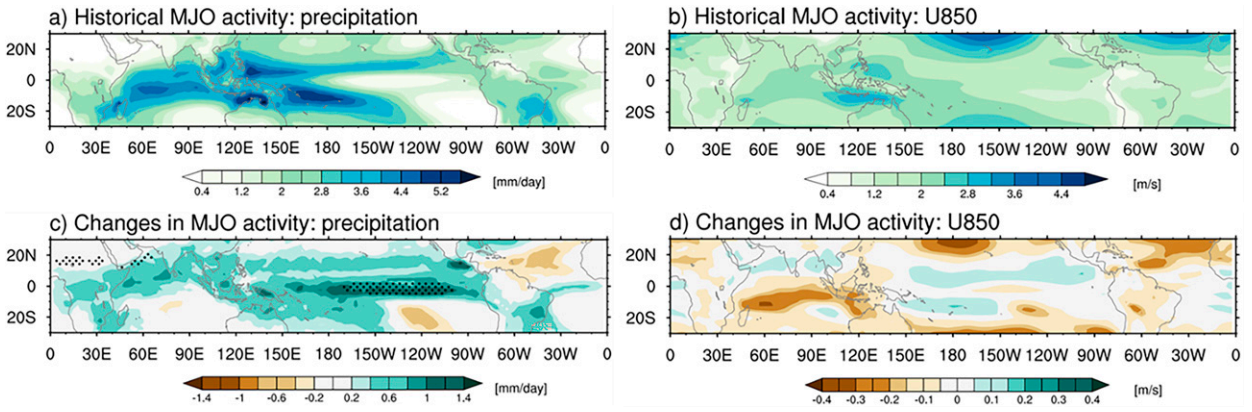

FIG. 7. MMM MJO activity represented by the standard deviation of (a) precipitation and (b) 850-hPa zonal wind (U850) filtered anomalies over the historical period. (c),(d) The difference of MJO activity between the future and historical period (future minus historical). Dots indicate regions where the difference exceeds the 95% confidence level according to the bootstrapping difference test.

activity in CMIP6s has a large bias, where the maximum activity is shifted toward the subtropics [Fig. 7b herein compared to Fig. 3 in Waliser et al. (2009)]. In the future, MJO precipitation is projected to be stronger over the northern Indian Ocean, Maritime Continent, and western Pacific, and extends eastward to the eastern Pacific (Fig. 7c), where the increase in precipitation activity is significant over 95% confidence level. These MJO changes are consistent with previous modeling studies (e.g., Arnold et al. 2015; Bui and Maloney 2018, 2020; Maloney et al. 2019; Zhou et al. 2020). A reconstruction of MJO activity using tropical surface pressures in Oliver and Thompson (2011) also showed a 13% increase in MJO amplitude over the last century. On the other hand, MJO circulation would be modestly weaker in the Indian Ocean and stronger in the Pacific, although the projected changes are insignificant (Fig. 7d). This indicates that MJO precipitation and circulation will change differently: the MJO precipitation is projected to be significantly stronger over most of the Indo-Pacific warm pool, while MJO circulation has no significant changes, consistent with Zhou et al. (2020).

In addition to the MJO, the basic state, and especially the westerly jet, influences MJO teleconnections by altering teleconnection pathways (Wang et al. 2020b). To examine the impact of the jet on future teleconnections, the climatology of U250 in the historical and future periods are compared (Fig. 8). The MMM shows an eastward extended jet in future climate, consistent with Zhou et al. (2020), and a poleward extension and weaker amplitude in the jet core region (Fig. 8a). These changes are further quantified using the basic state metrics developed in Wang et al. (2020b) as follows. 1) The jet amplitude is calculated as the average of U250 climatology in the jet core region, defined as the 5° zonal and meridional extension from the maximum U250 center. The MMM shows a modest change (54.61 m s^{-1} in the historical run and 53.85 m s^{-1} in the future run), that is, a 1.4% decrease in the core region. 80% of the models project a significantly weaker subtropical jet in the core region in the future (Fig. 9a). 2) The zonal extension of the jet is quantified by calculating the U250-weighted longitude 10° north and south from the maximum jet center across the longitudinal span of 100°E–120°W. Larger values indicate more eastward extension of the jet, while smaller values indicate westward retraction. The historical MMM is 163.25°, and the future MMM is 164.62°, which amounts to a 1.4° more eastward extension in the future jet. The significant eastward extension of the jet is projected by all models except in MPI-ESM1-2-LR (Fig. 9b). 3) The meridional shift of the jet is measured by calculating the U250-weighted latitude over 100°E–120°W, 10–60°N. The larger (smaller) the value, the more poleward (equatorward) the jet is positioned. A poleward shift of the jet (from ~35.2° to 35.5°N for the MMM; Fig. 9c) can be found in most models (80%) and is significant in nine models.

5. Mechanisms of future MJO teleconnection changes

In this section, mechanisms of future MJO teleconnection changes are examined using the LBM (Watanabe and Kimoto 2000). The main focus is on the eastward extension in MJO teleconnections as it is the most robust change in the future. Zhou et al. (2020) found that the eastward extension in future MJO teleconnections is primarily due to the eastward extension of the Pacific westerly jet. Here, we further examine the relative contributions of the MJO and jet changes to the Rossby wave generation and propagation by analyzing the anomalous RWS and propagation wave path. This will illustrate the dynamical processes through which the changes in the MJO and the basic state lead to the eastward extension in MJO teleconnections, which has not been well addressed in previous studies. The primitive equations of the LBM are identical to those in the atmospheric general circulation model (AGCM) developed at the Center for Climate System Research, University of Tokyo, Japan, and the National Institute for Environmental Studies, but linearized by a basic state. The model has a horizontal resolution of T42 (~2.8° grid resolution) and 20 unevenly spaced vertical sigma levels. The magnitude of the biharmonic diffusion coefficient and the dissipation time scale for Newtonian damping and Rayleigh friction are set according to Wang et al. (2020b).

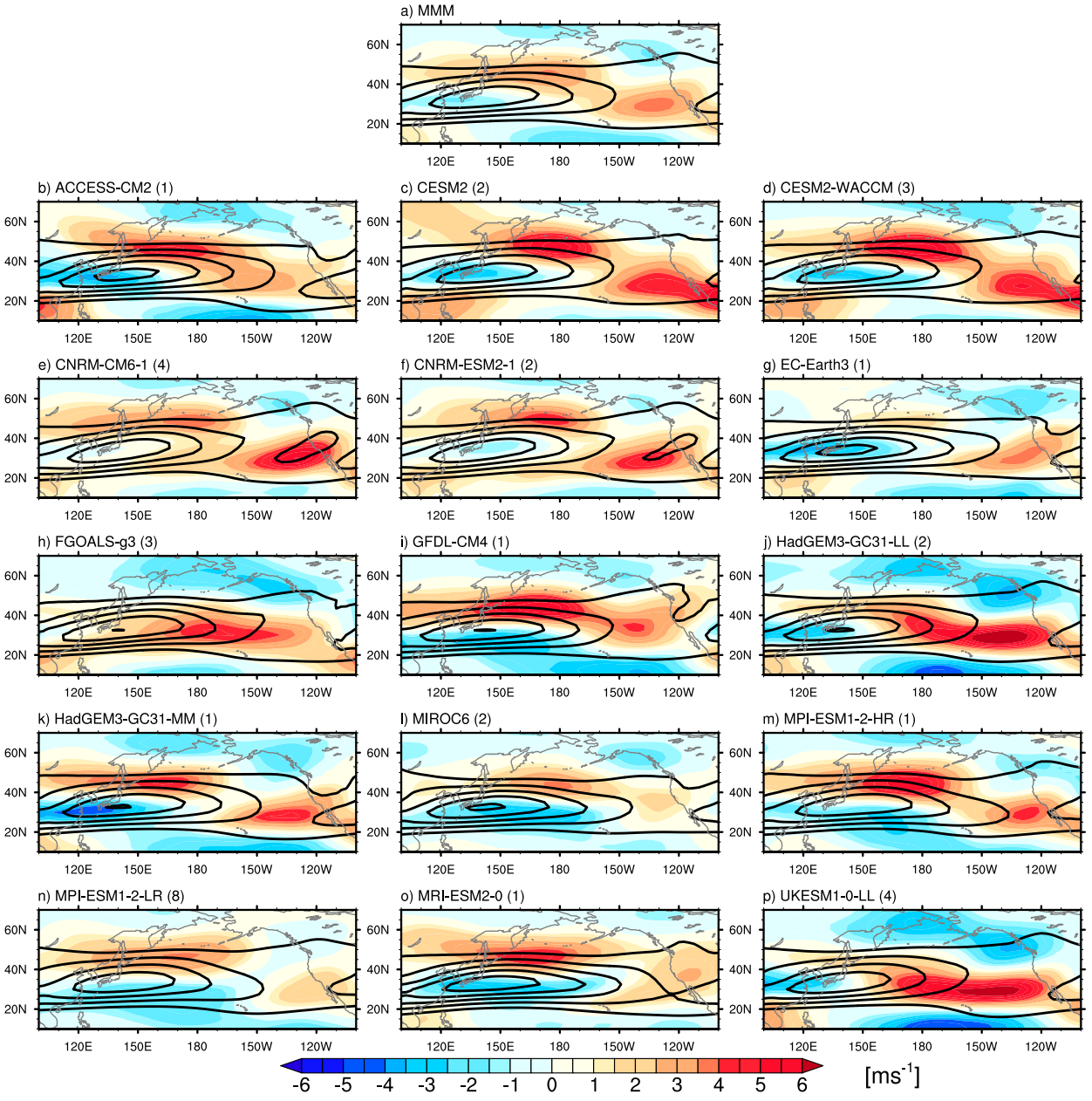

FIG. 8. Climatology of U250 (contour interval: 10 m s^{-1} starting from 20 m s^{-1}) in the CMIP6 historical runs for the (a) MMM and (b)–(p) individual models. Shading denotes the future changes in the jet, defined as the difference between the future and historical U250.

The linear response to a prescribed MJO heating is derived to examine MJO teleconnections (Mori and Watanabe 2008; Henderson et al. 2017; Wang et al. 2020b). In the control run, the LBM is forced by the historical MJO and historical basic state. The basic state uses the October to March climatology (including geopotential height, relative and specific humidity, temperature, winds, and surface pressure) generated from the historical MMM throughout 1979–2014. The MJO forcing is constructed by converting the precipitation rate to the latent heating ($Q_1 \approx LP$, where L represents the latent heat of condensation and P represents the amount of precipitation), which is the dominant component in the apparent heat source Q_1 (Yanai et al. 1973). We do not use the full equation of Q_1 because some models do not provide variables required for the calculation. The vertical profile of the MJO heating is in the form of $(1 - \sigma)\sin[\pi(1 - \sigma)]$ with a peak at $\sigma = 0.35$, and its vertical average is equivalent to latent heating (LP) estimated from MJO precipitation (e.g., Jin and Hoskins 1995). This simplified MJO heating generates realistic teleconnection patterns (e.g., Seo and Son 2012; Seo and Lee 2017). The model is run for 30 days and the MJO forcing is switched off after the first 5 days. The MJO forcing is constructed based on

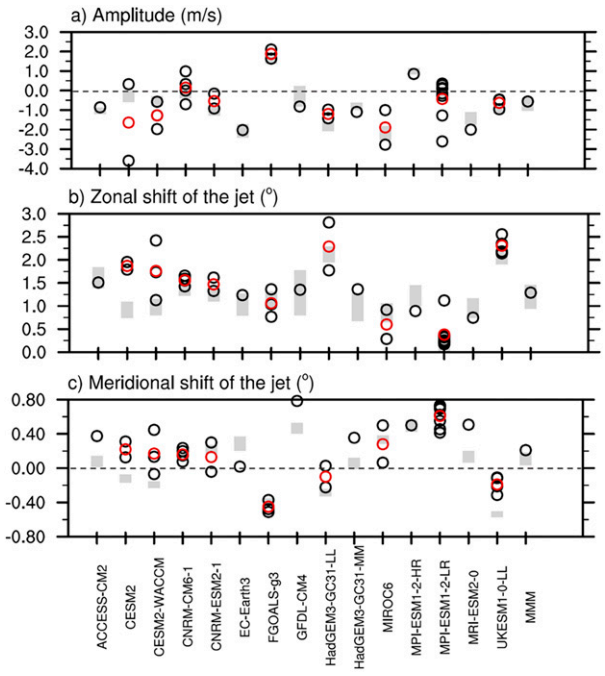

FIG. 9. Absolute change (future minus historical) of jet (a) amplitude, (b) zonal position, and (c) meridional position. Black open circles represent the results for individual ensembles or the MMM. Red open circles indicate the ensemble mean. Gray bars indicate the 95% confidence interval of the bootstrapping test.

the MJO phase 3 precipitation patterns as follows: First, a propagating MJO is derived by linearly interpolating the eight MJO phases to 40-day MJO propagation using the MMM following Henderson et al. (2017) and Wang et al. (2020b), assuming an average duration of 5 days per phase. This allows for the evolvement of the MJO pattern within one phase and a smooth transition during the MJO life cycle. Then, MJO propagation from phase 3 to phase 4 (day 11–15) is extracted and used as the MJO forcing. This enables us to examine a quasi-stationary teleconnection response in the LBM but maintain the MJO propagation feature in the meantime. Note that using the entire life cycle of MJO propagation led to a similar teleconnection response in the LBM, but making it hard to determine the role of the RWS which will be strongly influenced by the previous MJO phases. We confine the heating anomalies to 30°S–30°N to exclude the extratropical influence and focus on the tropical forcing.

The LBM phase 3 MJO teleconnection (referred to as P3_Z500a) is defined as the day 11–15 averaged Z500a response to the MJO and basic state forcing, which is equivalent to the lagged 10–14-day averaged response to the MJO heating over the eastern Indian Ocean and western Pacific. Days 11–15 are chosen to derive a quasi-stationary teleconnection response, which is found to be the lag time when the LBM response resembles the observed pattern (Tseng et al. 2019). The P3_Z500a in the current climate is simulated by forcing the LBM with the historical MJO and historical basic state (HIST run) as shown in Fig. 10a. Its spatial pattern is highly consistent with the observed Z500a pattern (Fig. 1a), with a pattern CC calculated over the PNA region of 0.84. The future P3_500a is derived by forcing the LBM with the MMM MJO and basic state derived from CMIP6 SSP585 runs (SSP run), and the results are shown in Fig. 10b. The LBM captures the eastward extended MJO teleconnections over the North Pacific and the weaker amplitude over North America as found in CMIP6s (section 3). The Z500a east–west position in the HIST run is 184.5° and shifts to 188.2° in

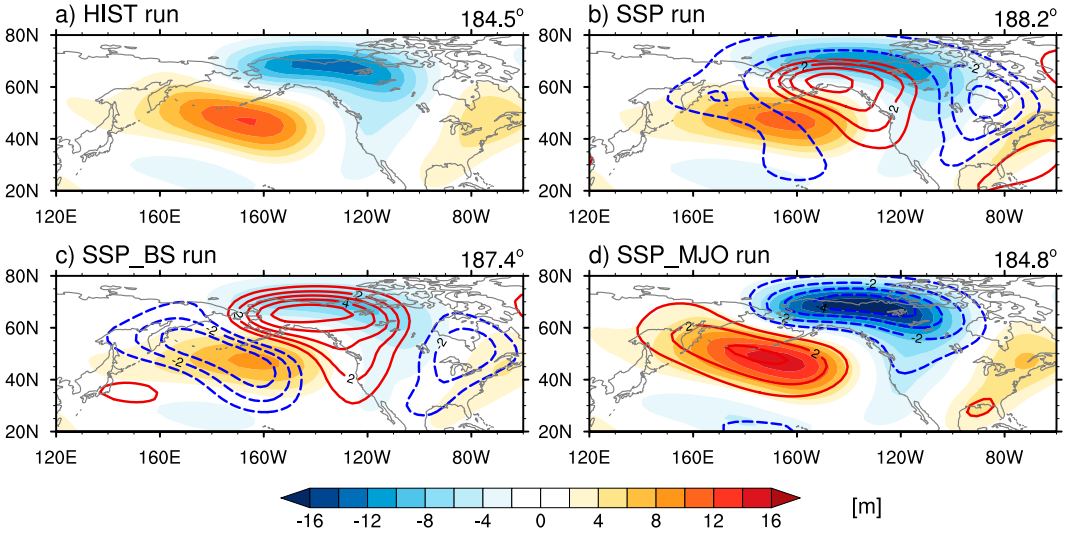

FIG. 10. (a) LBM phase 3 MJO teleconnections (P3_Z500a; shading) in the HIST run forced by the historical MJO and basic state. (b)–(d) As in (a), but for the (b) SSP run forced by the future MJO and basic state, (c) SSP_BS run forced only with the future basic state, and (d) SSP_MJO run forced only with the future MJO. Contours in (b)–(d) are the differences of P3_Z500a between the corresponding sensitivity experiments and the HIST run. Values at the top right of each figure indicate the east–west location of P3_Z500a over the North Pacific.

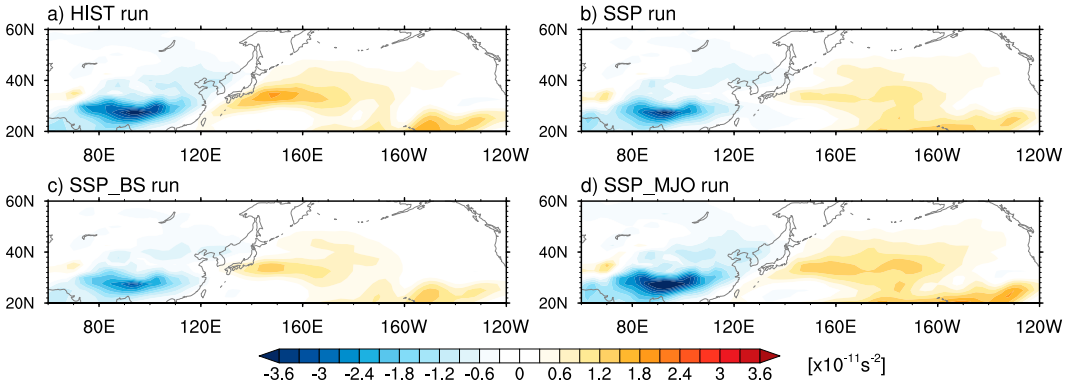

FIG. 11. Anomalous RWS at LBM day 2 in the (a) HIST, (b) SSP, (c) SSP_BS, and (d) SSP_MJO run.

the SSP run. To examine the relative impact of the MJO and basic state on MJO teleconnections, two additional experiments are carried out following Zhou et al. (2020). The first experiment uses the future basic state with the historical MJO (SSP_BS run; Fig. 10c), while the second experiment uses the future MJO with the historical basic state (SSP_MJO run; Fig. 10d). These experiments thus isolate the basic state and MJO contribution to future MJO teleconnection changes, respectively. In the SSP_BS run, position changes in MJO teleconnections are similar to the SSP run (i.e., MJO teleconnections extend ~3° eastward). However, in the SSP_MJO run, the eastward extension of MJO teleconnections is negligible (0.3° eastward). This is consistent with Zhou et al. (2020) that the eastward extension in future MJO teleconnections is mainly due to changes in the basic state. On the other hand, the MJO and basic state contribute differently to the teleconnection amplitude changes. The future basic state tends to weaken the teleconnection amplitude over the entire PNA region (Fig. 10c), which is consistent with Wolding et al. (2017) and Jenney et al. (2021). The stronger future MJO, on the other hand, leads to stronger MJO teleconnections (Fig. 10d). Therefore, due to the cancellation effect between the MJO and basic state, the future amplitude change is more uncertain and has regional variations as discussed in section 3.

Changes in future MJO teleconnections are determined by both changes in wave generation and wave propagation. To understand the mechanisms of the future eastward extension in MJO teleconnections, we first investigate the wave generation via anomalous RWS given as

$$\mathrm{RWS} = \left(-\overline{\xi}\nabla\cdot\mathbf{V}'_\chi - \xi'\nabla\cdot\overline{\mathbf{V}_\chi}\right) + \left(-\mathbf{V}'_\chi\cdot\nabla\overline{\xi} - \overline{\mathbf{V}_\chi}\cdot\nabla\xi'\right), \quad (1)$$

where $\mathbf{V}_\chi$ is the divergent component of horizontal winds, ξ is the absolute vorticity, primes represent the anomalies, and overbars denote the seasonal climatology. Figure 11a shows the anomalous RWS at 250 hPa at model day 2 in the HIST run. In response to the enhanced convection over the Indian Ocean and suppressed convection over the western Pacific, a maximum negative RWS over southern Asia and a positive RWS over the northwestern Pacific are simulated near the Pacific subtropical jet where the relative vorticity gradient is the largest (e.g., Hsu 1994; Seo and Lee 2017). The anomalous RWS pattern is dominated by the vorticity advection by divergent winds [third and fourth terms in Eq. (1)] as found in Hsu (1996) when the tropical divergence dominates in the first few days in the LBM. According to Hsu (1996), this anomalous RWS in the northwestern Pacific can persist up to 20 days and thus lead to a stationary response in the midlatitudes. In the SSP run (Fig. 11b), the RWS is weaker and more diffused, which seems to be associated primarily with the future changes in the basic state (Fig. 11c). The positive RWS shifts eastward to the central North Pacific, leading to an eastward teleconnection generation in the future. This eastward-shifted RWS in the Pacific is primarily attributed to the eastward extension in the MJO rather than the jet (Figs. 11c,d). This indicates that the future eastward extension in the MJO is the main contributor to the eastward MJO teleconnection generation. This finding does not contradict Zhou et al. (2020) because here we indicate the importance of the MJO in generating a more eastward shifted RWS while Zhou et al. (2020) analyzed the ultimate teleconnection pattern (same as Fig. 10). The eastward wave generation shown here does not necessarily lead to an eastward extension in the teleconnection pattern as the ultimate teleconnection pattern is determined by both the wave generation and propagation.

To compare the wave propagation between the current and future climate, the ray path of Rossby wave propagation generated by the anomalous RWS is tracked. According to ray theory (Hoskins and Karoly 1981), the dispersion relationship for the barotropic Rossby wave on the Mercator coordinate under a zonally invariant flow with no meridional wind is derived from the nondivergent barotropic vorticity equation given as

$$\omega = \overline{U}_M - \frac{\beta_M k}{k^2 + l^2}, \quad (2)$$

where ω is the angular frequency, k and l are zonal and meridional wavenumber, respectively, $\overline{U}_M$ is the mean zonal wind divided by the cosine of latitude, and β_M is equivalent to $\beta^* = (\partial f/\partial y) - (\partial^2\overline{u}/\partial y^2)$ defined as the meridional gradient

of absolute vorticity on a sphere multiplied by the cosine of latitude:

$$\beta_M = \cos\varphi \frac{1}{a}\frac{\partial \zeta_a}{\partial \varphi} = \left[2\Omega - \left(\frac{1}{\cos\varphi}\frac{\partial}{\partial\varphi}\right)^2\left(\frac{\cos^2\varphi \overline{U}_M}{a}\right)\right]\frac{\cos^2\varphi}{a}, \tag{3}$$

where ζ_a is the absolute vorticity and Ω is Earth's rotation rate. Equation (2) is satisfied for quasigeostrophic flow in the upper troposphere where the atmosphere is mostly barotropic, and thus it is suitable to be used in this study for tracking the ray paths entering the midlatitudes at 250 hPa (e.g., Seo and Lee 2017; Li et al. 2020). The zonal and meridional group velocity is derived from Eq. (2), given as

$$\frac{dx}{dt} = C_{gx} = \overline{U}_M + \frac{\beta_M(k^2 - l^2)}{K_s^4}, \tag{4}$$

$$\frac{dy}{dt} = C_{gy} = \frac{2kl\beta_M}{K_s^4}. \tag{5}$$

The ray path is derived by integrating Eqs. (4) and (5) using the fourth-order Runge–Kutta method (Seo and Lee 2017). Note that meridional wavenumber in Eqs. (4) and (5) is derived from Eq. (2) in which ω is zero for the stationary Rossby waves and zonal wavenumber remains constant along the ray. The anomalous RWS at 250 hPa at model day 2 (Fig. 11) greater/smaller than $\pm 1 \times 10^{-11}$ s^2 is used as the starting point for individual rays. Waves with zonal wavenumber $k = 1, 2, 3, 4$ are tracked for 10 days. These spatial scales are consistent with the convective scales of the MJO and are responsible for the formation of the PNA-like MJO teleconnection pattern (Seo and Lee 2017; Tseng et al. 2020). A total of 300–700 different rays are tracked in each MJO and basic state combination. During the ray tracing, the anomalous RWS is derived from each LBM experiment shown in Fig. 11. Following Tseng et al. (2020), the density of the ray paths over the region 60°E–80°W, 0°–80°N is calculated as the number of rays that pass each grid point divided by the total number of rays that are being tracked.

Figure 12a shows the density of ray paths of zonal wavenumber $k = 1, 2, 3, 4$ in the HIST run. The spatial distribution is consistent with ray theory and can be explained with the distribution of stationary wavenumber $K_S = a\left(\beta_M/\overline{U}_M\right)^{1/2}$ over the historical period in the MMM (Fig. 13a) that 1) higher ray path density is found within the subtropical jet where large wave trapping occurs due to the wave refraction toward high K_S; 2) waves propagate eastward along the subtropical jet and then northward toward the PNA region along a great circle path when they reach the jet exit region; and 3) waves reflect at a turning latitude where zonal wavenumber k equals to K_S and is absorbed at a critical latitude in the Indian Ocean and western Pacific where the mean zonal wind is easterly.

In the SSP run (Fig. 12b), the ray path density is extended eastward near the jet exit region (yellow shading in 170°–120°W, 20°–40°N), suggesting a more eastward wave propagation in the future climate. The relative role of the MJO and basic state is compared in Figs. 12c and 12d. When the LBM is forced with the future basic state and historical MJO (SSP_BS run; Fig. 12c), waves propagate farther eastward along the jet before reaching the jet exit (Fig. 12c) as indicated by the clear path of more eastward wave propagation in 180°–100°W, 20°–45°N similar to the SSP run. This leads to the eastward shift in MJO teleconnections in the SSP_BS run (Fig. 10c). On the other hand, when the LBM is forced with the future MJO and historical basic state (SSP_MJO run; Fig. 12d), a strong increase in ray path density is found within the jet near 170°W due to the eastward shift of anomalous RWS. However, waves that are excited from this eastward-shifted RWS tend to propagate directly northward into North America, thus having little impact on the eastward shift of teleconnections (Fig. 10d).

Ray paths for zonal wavenumber 4 in the HIST and SSP run are shown in Figs. 12e and 12f along with anomalous RWS to visualize the differences in wave propagation between the current and future climate. We specifically show this wave scale as it has the most significant changes in the zonal propagation among the zonal wavenumbers we analyzed (not shown). The short waves are also modulated more by the subtropical jet. The main difference found in the SSP run compared to the HIST run is that waves are propagating more eastward and slightly more poleward before reaching the turning latitude (i.e., wave propagation generally extends more northeastward in the future). The mechanisms of these changes can be further explained as follows with the differences in K_S (Fig. 13). Because of the eastward extended MJO propagation, the anomalous RWS generation is shifted eastward (Fig. 11), leading to the eastward generation of MJO teleconnections. The eastward extended jet leads to the eastward extension of $\beta_M < 0$ regions that can be found in all CMIP6 models (Fig. 13), causing more eastward wave propagation before they propagate meridionally. The weaker westerly waveguide in most CMIP6 models (~80%; Fig. 13) leads to weaker wave refractions toward the jet and hence more poleward propagation of MJO teleconnections. These future changes in the Rossby wave generation and propagation lead to a robust eastward extension and slight northward extension of MJO teleconnections, as projected by most CMIP6s.

In summary, in this section, we examined the relative contribution of the MJO and basic state to future MJO teleconnection changes (Figs. 10–12). If the future changes are solely from the MJO, the wave generation (anomalous RWS) shifts eastward and waves propagate directly northward into North America because they are generated near the jet exit (Figs. 11d and 12d). Therefore, there is only a subtle change in the ultimate east–west location of MJO teleconnections (Fig. 10d). On the other hand, if there are only changes from the basic state, waves propagate farther eastward than they are in the current climate to exit the eastward extended jet (Figs. 11c and 12c). This eventually leads to the more eastward extension of MJO teleconnections in the future (Fig. 10c). These results together confirm that the future basic state change plays a more important role in MJO teleconnection changes, consistent with Zhou et al. (2020). Results in this study provide plausible dynamical processes for this future MJO teleconnection change.

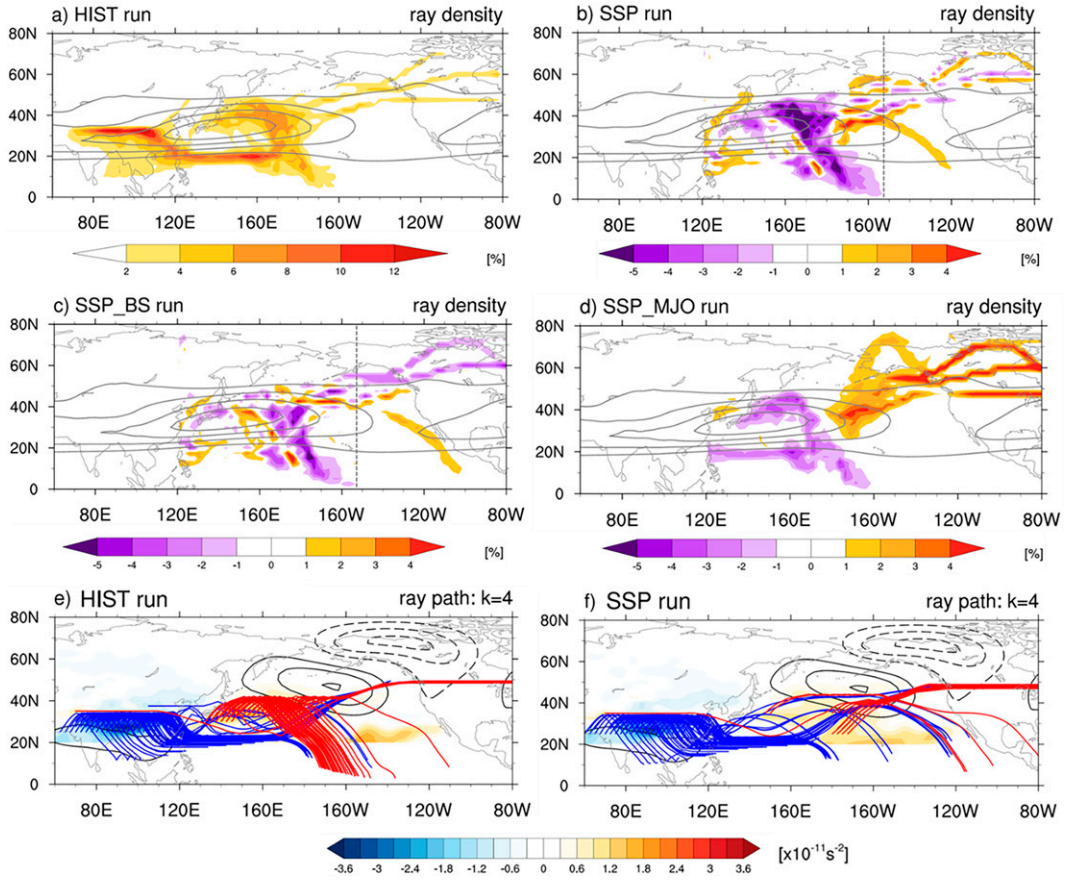

FIG. 12. (a)–(d) The Rossby wave ray density (%) in the four LBM experiments for zonal wavenumber $k = 1, 2, 3, 4$. Shading in (b)–(d) represents the difference of ray path density between the corresponding sensitivity experiment and the HIST run. (e),(f) Anomalous RWS at LBM day 2 (shading, only anomalies poleward of 20°N are shown) and Rossby wave ray path for zonal wavenumber 4 in the (e) HIST run and (f) SSP run. Blue (red) lines denote the ray path at day 10 excited from the negative (positive) anomalous RWS at day 2 (shadings) in southern Asia (the western North Pacific). Contours represent P3_Z500a (interval: 4 m), which are the same as the shading in Fig. 10a. Vertical lines in (b) and (c) denote the eastern boundary of the westerly jet in the current climate [i.e., the jet in (a) and (d)].

6. Summary and discussion

In this study, we examined future changes in boreal winter MJO teleconnections over the PNA region in 15 CMIP6 models. Most models project an eastward and northward extension in MJO teleconnections over the North Pacific and a weaker amplitude over North America with larger consistency between individual MJO events and modest shorter persistence in a warming climate. The eastward extension is found to be the most significant change in the future followed by the northward extension and larger pattern consistency, while other changes are more dominated by the atmospheric internal variability with a large model spread. The causes of future MJO teleconnection changes are explored by examining changes in the future MJO and basic state. Future MJO activity is stronger in the precipitation field over the Indo-Pacific region, with the largest and most significant intensification projected to occur over the eastern Pacific. The subtropical westerly jet becomes weaker in the core region and extends eastward and poleward.

Previous studies have argued that the MJO teleconnection shifts eastward with the jet exit as it is anchored on the jet exit through the barotropic conversion. In this study, we further examine the relative impacts of the MJO and basic state on wave generation and wave propagation by performing various LBM experiments. The results of the anomalous RWS and wave propagation mechanisms are used to explain the eastward extension of future MJO teleconnections. Key findings are summarized in Fig. 14 for MJO phase 3. The MJO convection is indicated by the cloud-shape patterns. In the current climate (Fig. 14a), the enhanced MJO convection is located over the eastern Indian Ocean and suppressed convection over the western Pacific. In response to the interaction between the dipole MJO convection and the large absolute vorticity gradient near the westerly jet, negative anomalous RWS are excited over South Asia and positive anomalous RWS over the western Pacific. At the northern and southern sides of the subtropical jet, the meridional gradient of absolute vorticity reverses ($\beta_M < 0$) and the Rossby waves cannot

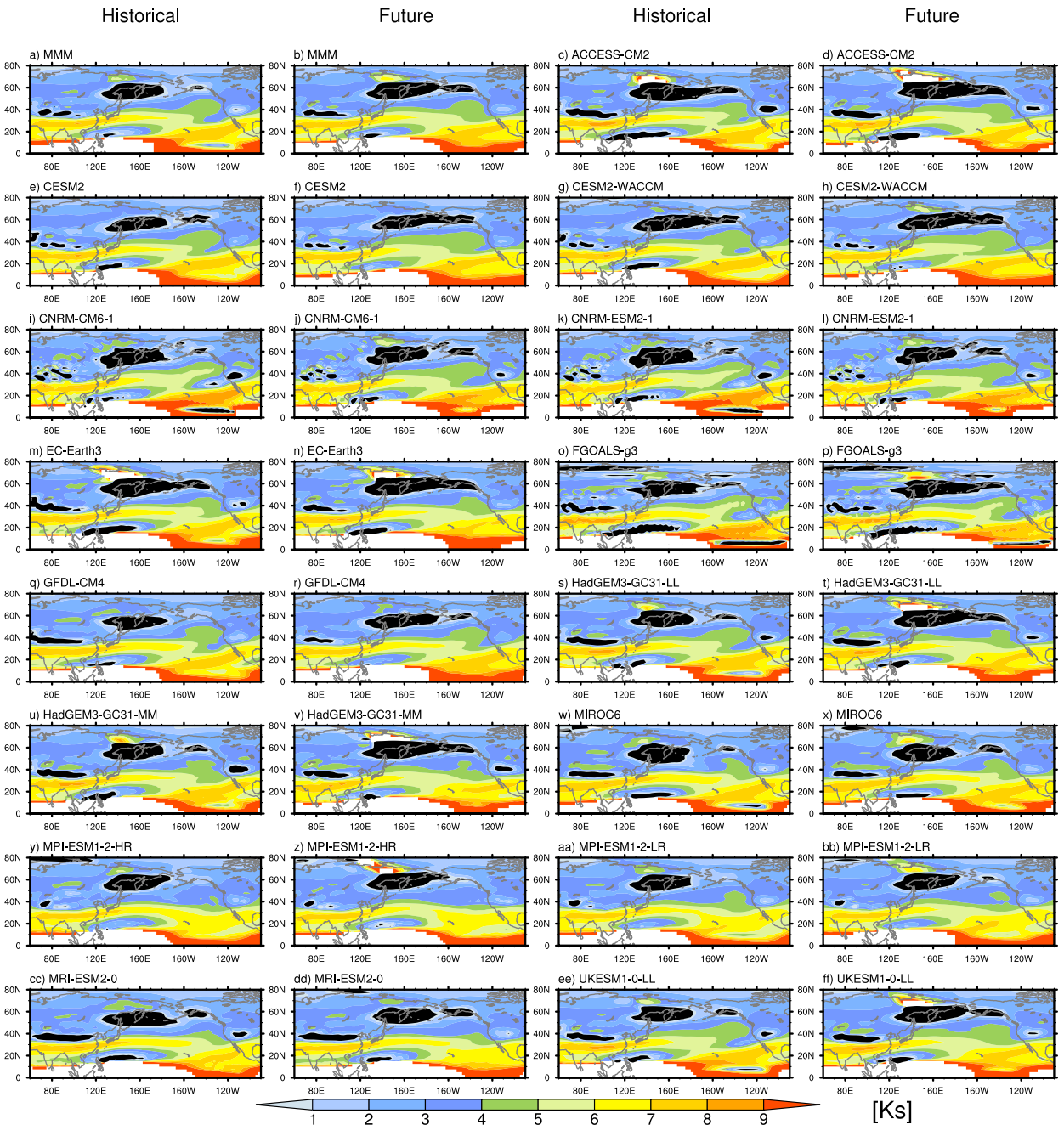

FIG. 13. MMM stationary wavenumber K_S derived from climatological U250 on Mercator coordinates for the (a) historical and (b) future period. Black areas are where the meridional gradient of absolute vorticity β_M is negative. Regions of easterly zonal winds are in white. Historical and future K_S in the individual models are shown in (c)–(ff).

propagate through those turning latitudes. The westerly jet, where the stationary wavenumber is large, acts as a waveguide, leading to an eastward propagation of Rossby waves along the jet which emanates into the extratropical regions at the jet exit region. Future changes in the above dynamical processes are manifested as follows (Fig. 14b): 1) the eastward extended MJO induces eastward shifted anomalous RWS, which leads to the eastward generation of MJO teleconnections, and 2) the eastward extended westerly jet induces eastward extended regions of $\beta_M < 0$, which leads to more eastward propagation of MJO teleconnections.

This study extends the previous work of understanding boreal winter MJO teleconnections under a changing climate by further quantifying the uncertainty of changes including the intra- and intermodel uncertainty and regional differences. We also examined the changes in the dynamical

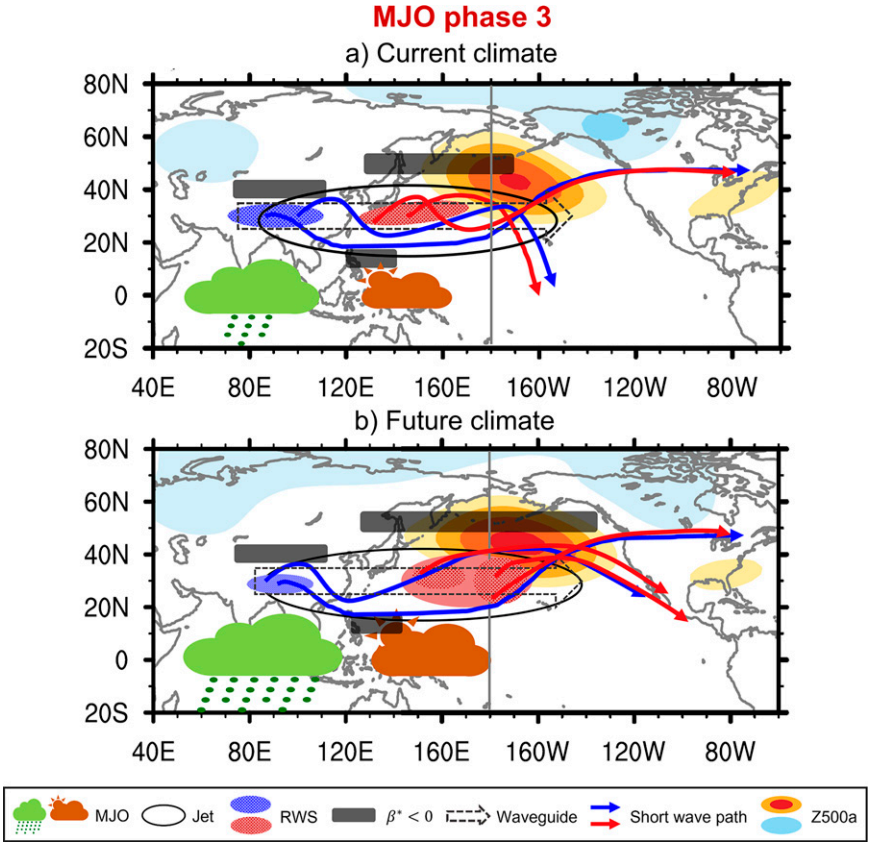

FIG. 14. The schematic diagram of dynamical processes (RWS and Rossby wave propagation) related to MJO teleconnections during MJO phase 3 in the (a) current and (b) future climate. Results are derived from the MMM of CMIP6 historical and future runs. The vertical gray line indicates the "dateline." The relative magnitude of each component is indicated by the difference in the thickness, length, or size of the graph. Note that the variables (e.g., anomalous RWS and propagation wave path) may not be entirely precise in location and pattern.

processes such as anomalous RWS and propagation wave path associated with the teleconnection changes and explored the relative contributions of the future MJO and basic state to these changes. The findings have implications on the predictability of MJO-related weather phenomena in the future climate. For example, we showed that MJO teleconnections may be more consistent between different MJO events in the future, leading to possibly more reliable S2S predictions for weather phenomena such as precipitation extremes, atmospheric rivers, and heat waves in the extratropics as they are highly modulated by MJO teleconnections (e.g., Lee and Grotjahn 2019; Zhou et al. 2021). The more eastward extension in MJO teleconnections also leads to greater MJO impacts on the northeastern Pacific and North America such as a 54% increase in MJO-induced precipitation variability over California (Zhou et al. 2020). More research on the plausible impacts of future teleconnection changes is encouraged.

Previous studies have demonstrated that changes in tropical sea surface temperature (SST) patterns are important for determining the future changes in the MJO intensity and eastward extension of the MJO and subtropical jet (e.g., Subramanian et al. 2014; Chang et al. 2015; Allen and Luptowitz 2017; Zhou et al. 2020). How the uncertainty in the projected SST pattern leads to MJO and its teleconnection uncertainty requires further investigation. In addition to the tropical SST pattern, the MJO and subtropical jet are also modulated by the quasi-biennial oscillation (QBO; Yoo and Son 2016; Wang et al. 2018; Martin et al. 2021). The difference in model ability in simulating the QBO–MJO connection may also lead to uncertainty in future MJO and teleconnection projections, which merits investigation in future studies.

Acknowledgments. Constructive and valuable comments from Editor Dr. Isla Ruth Simpson and three anonymous reviewers are greatly appreciated. We thank Dr. Daehyun Kim and Daehyun Kang for providing the CFSR, MERRA-2, and JRA-55 reanalysis data. We thank Dr. Kyong-Hwan Seo for the discussion of the Rossby wave path calculation. We also thank Dr. Eric D. Maloney and Edmund K.M. Chang for their valuable comments. Wang was supported by NSF Grant AGS-1652289 and the California Department of Water Resources AR Program (Grant 4600013361). Kim

was supported by NSF Grant AGS-1652289 and KMA R&D Program Grant KMI2021-01210. DeFlorio was supported by the California Department of Water Resources AR Program (Grant 4600013361).

Data availability statement. The ERA5 data were obtained from the Copernicus Climate Change Service Climate Data Store (CDS) via https://cds.climate.copernicus.eu/cdsapp#!/dataset/reanalysis-era5-single-levels?tab=form (Hersbach et al. 2020). The CMIP6 model output was downloaded from the CMIP6 archives at https://esgf-node.llnl.gov/projects/cmip6/ (O'Neill et al. 2016). The observational outgoing longwave radiation dataset was obtained from NOAA PSL available at https://psl.noaa.gov/data/gridded/data.interp_OLR.html. The CFSR, MERRA-2, and JRA-55 data were provided by Dr. Daehyun Kim and Daehyun Kang.

REFERENCES

Adames, Á. F., D. Kim, A. H. Sobel, A. Del Genio, and J. Wu, 2017: Changes in the structure and propagation of the MJO with increasing CO_2. *J. Adv. Model. Earth Syst.*, **9**, 1251–1268, https://doi.org/10.1002/2017MS000913.

Ahn, M.-S., and Coauthors, 2020: MJO propagation across the Maritime Continent: Are CMIP6 models better than CMIP5 models? *Geophys. Res. Lett.*, **47**, e2020GL087250, https://doi.org/10.1029/2020GL087250.

Allen, R. J., and R. Luptowitz, 2017: El Niño-like teleconnection increases California precipitation in response to warming. *Nat. Commun.*, **8**, 16055, https://doi.org/10.1038/ncomms16055.

Arnold, N. P., M. Branson, Z. Kuang, D. A. Randall, and E. Tziperman, 2015: MJO intensification with warming in the superparameterized CESM. *J. Climate*, **28**, 2706–2724, https://doi.org/10.1175/JCLI-D-14-00494.1.

Bui, H. X., and E. D. Maloney, 2018: Changes in Madden–Julian oscillation precipitation and wind variance under global warming. *Geophys. Res. Lett.*, **45**, 7148–7155, https://doi.org/10.1029/2018GL078504.

——, and ——, 2019a: Mechanisms for global warming impacts on Madden–Julian oscillation precipitation amplitude. *J. Climate*, **32**, 6961–6975, https://doi.org/10.1175/JCLI-D-19-0051.1.

——, and ——, 2019b: Transient response of MJO precipitation and circulation to greenhouse gas forcing. *Geophys. Res. Lett.*, **46**, 13 546–13 555, https://doi.org/10.1029/2019GL085328.

——, and ——, 2020: Changes to the Madden–Julian oscillation in coupled and uncoupled aquaplanet simulations with 4xCO2. *J. Adv. Model. Earth Syst.*, **12**, e2020MS002179, https://doi.org/10.1029/2020MS002179.

Carlson, H., and R. Caballero, 2016: Enhanced MJO and transition to superrotation in warm climates. *J. Adv. Model. Earth Syst.*, **8**, 304–318, https://doi.org/10.1002/2015MS000615.

Cassou, C., 2008: Intraseasonal interaction between the Madden–-Julian oscillation and the North Atlantic oscillation. *Nature*, **455**, 523–527, https://doi.org/10.1038/nature07286.

Chang, C. W. J., W. L. Tseng, H. H. Hsu, N. Keenlyside, and B. J. Tsuang, 2015: The Madden–Julian oscillation in a warmer world. *Geophys. Res. Lett.*, **42**, 6034–6042, https://doi.org/10.1002/2015GL065095.

Deng, Y., and T. Jiang, 2011: Intraseasonal modulation of the North Pacific storm track by tropical convection in boreal winter. *J. Climate*, **24**, 1122–1137, https://doi.org/10.1175/2010JCLI3676.1.

Eyring, V., S. Bony, G. A. Meehl, C. A. Senior, B. Stevens, R. J. Stouffer, and K. E. Taylor, 2016: Overview of the Coupled Model Intercomparison Project Phase 6 (CMIP6) experimental design and organization. *Geosci. Model Dev.*, **9**, 1937–1958, https://doi.org/10.5194/gmd-9-1937-2016.

Henderson, S. A., E. D. Maloney, and E. A. Barnes, 2016: The influence of the Madden–Julian oscillation on Northern Hemisphere winter blocking. *J. Climate*, **29**, 4597–4616, https://doi.org/10.1175/JCLI-D-15-0502.1.

——, ——, and S.-W. Son, 2017: Madden–Julian oscillation Pacific teleconnections: The impact of the basic state and MJO representation in general circulation models. *J. Climate*, **30**, 4567–4587, https://doi.org/10.1175/JCLI-D-16-0789.1.

Hersbach, H., and Coauthors, 2020: The ERA5 global reanalysis. *Quart. J. Roy. Meteor. Soc.*, **146**, 1999–2049, https://doi.org/10.1002/qj.3803.

Hoskins, B. J., and D. J. Karoly, 1981: The steady linear response of a spherical atmosphere to thermal and orographic forcing. *J. Atmos. Sci.*, **38**, 1179–1196, https://doi.org/10.1175/1520-0469(1981)038<1179:TSLROA>2.0.CO;2.

Hsu, H. H., 1994: Relationship between tropical heating and global circulation: Interannual variability. *J. Geophys. Res.*, **99**, 10 473–10 489, https://doi.org/10.1029/94JD00247.

——, 1996: Global view of the intraseasonal oscillation during northern winter. *J. Climate*, **9**, 2386–2406, https://doi.org/10.1175/1520-0442(1996)009<2386:GVOTIO>2.0.CO;2.

Jenney, A. M., D. A. Randall, and E. A. Barnes, 2021: Mechanisms driving MJO teleconnection changes with warming in CMIP6. *Wea. Climate Dyn.*, https://doi.org/10.5194/wcd-2021-9.

Jiang, X., and Coauthors, 2020: Fifty years of research on the Madden–Julian oscillation: Recent progress, challenges, and perspectives. *J. Geophys. Res. Atmos.*, **125**, e2019JD030911, https://doi.org/10.1029/2019JD030911.

Jin, F., and B. J. Hoskins, 1995: The direct response to tropical heating in a baroclinic atmosphere. *J. Atmos. Sci.*, **52**, 307–319, https://doi.org/10.1175/1520-0469(1995)052<0307:TDRTTH>2.0.CO;2.

Kobayashi, S., and Coauthors, 2015: The JRA-55 reanalysis: General specifications and basic characteristics. *J. Meteor. Soc. Japan*, **93**, 5–48, https://doi.org/10.2151/jmsj.2015-001.

Lee, Y.-Y., and R. Grotjahn, 2019: Evidence of specific MJO phase occurrence with summertime California Central Valley extreme hot weather. *Adv. Atmos. Sci.*, **36**, 589–602, https://doi.org/10.1007/s00376-019-8167-1.

Li, R. K., T. Woollings, C. O'Reilly, and A. A. Scaife, 2020: Effect of the North Pacific tropospheric waveguide on the fidelity of model El Niño teleconnections. *J. Climate*, **33**, 5223–5237, https://doi.org/10.1175/JCLI-D-19-0156.1.

Liebmann, B., and C. A. Smith, 1996: Description of a complete (interpolated) outgoing longwave radiation dataset. *Bull. Amer. Meteor. Soc.*, **77**, 1275–1277, https://doi.org/10.1175/1520-0477-77.6.1274.

Lin, H., G. Brunet, and J. Derome, 2009: An observed connection between the North Atlantic oscillation and the Madden–Julian oscillation. *J. Climate*, **22**, 364–380, https://doi.org/10.1175/2008JCLI2515.1.

Liu, P., 2013: Changes in a modeled MJO with idealized global warming. *Climate Dyn.*, **40**, 761–773, https://doi.org/10.1007/s00382-012-1323-2.

Madden, R. A., and P. Julian, 1971: Detection of a 40–50 day oscillation in the zonal wind in the tropical Pacific. *J. Atmos.*

Sci., **28**, 702–708, https://doi.org/10.1175/1520-0469(1971)028<0702:DOADOI>2.0.CO;2.

——, and ——, 1972: Description of a global-scale circulation cells in the tropics with a 40–50 day period. *J. Atmos. Sci.*, **29**, 1109–1123, https://doi.org/10.1175/1520-0469(1972)029<1109:DOGSCC>2.0.CO;2.

Maloney, E. D., A. F. Adames, and H. X. Bui, 2019: Madden–Julian oscillation changes under anthropogenic warming. *Nat. Climate Change*, **9**, 26–33, https://doi.org/10.1038/s41558-018-0331-6.

Martin, Z., and Coauthors, 2021: The influence of the quasi-biennial oscillation on the Madden–Julian oscillation. *Nat. Rev. Earth Environ.*, **2**, 477–489, https://doi.org/10.1038/s43017-021-00173-9.

Molod, A., L. Takacs, M. Suarez, and J. Bacmeister, 2015: Development of the GEOS-5 atmospheric general circulation model: Evolution from MERRA to MERRA2. *Geosci. Model Dev.*, **8**, 1339–1356, https://doi.org/10.5194/gmd-8-1339-2015.

Mori, M., and M. Watanabe, 2008: The growth and triggering mechanisms of the PNA: A MJO-PNA coherence. *J. Meteor. Soc. Japan*, **86**, 213–236, https://doi.org/10.2151/jmsj.86.213.

Mundhenk, B. D., E. A. Barnes, and E. D. Maloney, 2016: All-season climatology and variability of atmospheric river frequencies over the North Pacific. *J. Climate*, **29**, 4885–4903, https://doi.org/10.1175/JCLI-D-15-0655.1.

Neelin, J. D., B. Langenbrunner, J. E. Meyerson, A. Hall, and N. Berg, 2013: California winter precipitation change under global warming in the Coupled Model Intercomparison Project phase 5 ensemble. *J. Climate*, **26**, 6238–6256, https://doi.org/10.1175/JCLI-D-12-00514.1.

Oliver, E. C., and K. R. Thompson, 2011: A reconstruction of Madden–Julian oscillation variability from 1905 to 2008. *J. Climate*, **25**, 1996–2019, https://doi.org/10.1175/JCLI-D-11-00154.1.

O'Neill, B. C., and Coauthors, 2016: The Scenario Model Intercomparison Project (ScenarioMIP) for CMIP6. *Geosci. Model Dev.*, **9**, 3461–3482, https://doi.org/10.5194/gmd-9-3461-2016.

Pritchard, M. S., and D. Yang, 2016: Response of the superparameterized Madden–Julian oscillation to extreme climate and basic-state variation challenges a moisture mode view. *J. Climate*, **29**, 4995–5008, https://doi.org/10.1175/JCLI-D-15-0790.1.

Saha, S., and Coauthors, 2010: The NCEP Climate Forecast System Reanalysis. *Bull. Amer. Meteor. Soc.*, **91**, 1015–1058, https://doi.org/10.1175/2010BAMS3001.1.

Samarasinghe, S. M., C. Connolly, E. A. Barnes, I. Ebert-Uphoff, and L. Sun, 2021: Strengthened causal connections between the MJO and the North Atlantic with climate warming. *Geophys. Res. Lett.*, **48**, e2020GL091168, https://doi.org/10.1029/2020GL091168.

Sardeshmukh, P. D., and B. J. Hoskins, 1988: The generation of global rotational flow by steady idealized tropical divergence. *J. Atmos. Sci.*, **45**, 1228–1251, https://doi.org/10.1175/1520-0469(1988)045<1228:TGOGRF>2.0.CO;2.

Seo, K.-H., and S.-W. Son, 2012: The global atmospheric circulation response to tropical diabatic heating associated with the Madden–Julian oscillation during northern winter. *J. Atmos. Sci.*, **69**, 79–96, https://doi.org/10.1175/2011JAS3686.1.

——, and H.-J. Lee, 2017: Mechanisms for a PNA-like teleconnection pattern in response to the MJO. *J. Atmos. Sci.*, **74**, 1767–1781, https://doi.org/10.1175/JAS-D-16-0343.1.

Simpson, I. R., R. Seager, M. Ting, and T. A. Shaw, 2016: Causes of change in Northern Hemisphere winter meridional winds and regional hydroclimate. *Nat. Climate Change*, **6**, 65–70, https://doi.org/10.1038/nclimate2783.

Stan, C., D. M. Straus, J. S. Frederiksen, H. Lin, E. D. Maloney, and C. Schumacher, 2017: Review of tropical–extratropical teleconnections on intraseasonal time scales. *Rev. Geophys.*, **55**, 902–937, https://doi.org/10.1002/2016RG000538.

Subramanian, A., M. Jochum, A. J. Miller, R. Neale, H. Seo, D. Waliser, and R. Murtugudde, 2014: The MJO and global warming: A study in CCSM4. *Climate Dyn.*, **42**, 2019–2031, https://doi.org/10.1007/s00382-013-1846-1.

Taylor, K. E., 2001: Summarizing multiple aspects of model performance in a single diagram. *J. Geophys. Res.*, **106**, 7183–7192, https://doi.org/10.1029/2000JD900719.

Tseng, K.-C., E. Maloney, and E. Barnes, 2019: The consistency of MJO teleconnection patterns: An explanation using linear Rossby wave theory. *J. Climate*, **32**, 531–548, https://doi.org/10.1175/JCLI-D-18-0211.1.

——, ——, and ——, 2020: The consistency of MJO teleconnection patterns on interannual time scales. *J. Climate*, **33**, 3471–3486, https://doi.org/10.1175/JCLI-D-19-0510.1.

Waliser, D., and Coauthors, 2009: MJO simulation diagnostics. *J. Climate*, **22**, 3006–3030, https://doi.org/10.1175/2008JCLI2731.1.

Wang, J., 2020: PNA-like MJO teleconnections: Metrics, dynamical processes, and future change. Ph.D. dissertation, State University of New York at Stony Brook, 24 pp.

——, H. M. Kim, and E. K. Chang, 2018: Interannual modulation of Northern Hemisphere winter storm tracks by the QBO. *Geophys. Res. Lett.*, **45**, 2786–2794, https://doi.org/10.1002/2017GL076929.

——, ——, D. Kim, S. A. Henderson, C. Stan, and E. D. Maloney, 2020a: MJO teleconnections over the PNA region in climate models. Part I: Performance- and process-based skill metrics. *J. Climate*, **33**, 1051–1067, https://doi.org/10.1175/JCLI-D-19-0253.1.

——, ——, ——, ——, ——, and ——, 2020b: MJO teleconnections over the PNA region in climate models. Part II: Impacts of the MJO and basic state. *J. Climate*, **33**, 5081–5101, https://doi.org/10.1175/JCLI-D-19-0865.1.

Watanabe, M., and M. Kimoto, 2000: Atmosphere–ocean thermal coupling in the North Atlantic: A positive feedback. *Quart. J. Roy. Meteor. Soc.*, **126**, 3343–3369, https://doi.org/10.1002/qj.49712657017.

Wheeler, M. C., and H. H. Hendon, 2004: An all-season real-time multivariate MJO index: Development of an index for monitoring and prediction. *Mon. Wea. Rev.*, **132**, 1917–1932, https://doi.org/10.1175/1520-0493(2004)132<1917:AARMMI>2.0.CO;2.

Wolding, B. O., E. D. Maloney, S. Henderson, and M. Branson, 2017: Climate change and the Madden–Julian oscillation: A vertically resolved weak temperature gradient analysis. *J. Adv. Model. Earth Syst.*, **9**, 307–331, https://doi.org/10.1002/2016MS000843.

Yanai, M., S. Esbensen, and J.-H. Chu, 1973: Determination of bulk properties of tropical cloud clusters from large-scale heat and moisture budgets. *J. Atmos. Sci.*, **30**, 611–627, https://doi.org/10.1175/1520-0469(1973)030<0611:DOBPOT>2.0.CO;2.

Yoo, C., and S. W. Son, 2016: Modulation of the boreal wintertime Madden–Julian oscillation by the stratospheric quasi-biennial oscillation. *Geophys. Res. Lett.*, **43**, 1392–1398, https://doi.org/10.1002/2016GL067762.

Zheng, C., and E. K.-M. Chang, 2019: The role of MJO propagation, lifetime, and intensity on modulating the temporal

evolution of the MJO extratropical response. *J. Geophys. Res. Atmos.*, **124**, 5352–5378, https://doi.org/10.1029/2019JD030258.

——, ——, H.-M. Kim, M. Zhang, and W. Wang, 2018: Impacts of the Madden–Julian oscillation on storm-track activity, surface air temperature, and precipitation over North America. *J. Climate*, **31**, 6113–6134, https://doi.org/10.1175/JCLI-D-17-0534.1.

Zhou, S., M. L'Heureux, S. Weaver, and A. Kumar, 2012: A composite study of the MJO influence on the surface air temperature and precipitation over the continental United States. *Climate Dyn.*, **38**, 1459–1471, https://doi.org/10.1007/s00382-011-1001-9.

Zhou, W., D. Yang, S.-P. Xie, and J. Ma, 2020: Amplified Madden–Julian oscillation impacts in the Pacific–North America region. *Nat. Climate Change*, **10**, 654–660, https://doi.org/10.1038/s41558-020-0814-0.

Zhou, Y., H. Kim, and D. E. Waliser, 2021: Atmospheric river lifecycle responses to the Madden–Julian oscillation. *Geophys. Res. Lett.*, **48**, e2020GL090983, https://doi.org/10.1029/2020GL090983.